

## POLITECNICO DI TORINO

Master of Science Course in Materials Engineering for Industry 4.0

Master's Degree Thesis

# Characterisation of IN718 Nickel Superalloy Powder Bed Fusion Laser Additive Manufacturing

**Supervisors** 

Dr. Damjan Klobčar

Dr. Emmy Yu Cao

Dr. Milena Salvo

Dr. Cédric Courbon

Dr. Daniele Ugues

Candidate

Saikrishna Suresh Kumar

September 2025

# Erasmus Mundus Joint Master in Manufacturing 4.0 by IntElligent and SusTAinable Technologies



#### MASTER's Degree Thesis

# Characterisation of IN718 Nickel Superalloy Powder Bed Fusion Laser Additive Manufacturing

Supervisors

Prof. Damjan KLOBČAR

Prof. Emmy Yu CAO

Prof. Milena SALVO

Prof. Daniele UGUES

Prof. Cédric COURBON

Candidate

SAIKRISHNA Suresh Kumar

September 2025













#### Acknowledgment

I would like to extend my gratitude to my supervisors Dr Damjan Klobcar from University of Ljubljana and to Dr Emmy Yu Cao of Chalmers University for giving me this opportunity and inviting me to participate on this ongoing project at Chalmers University, I appreciate in her trust for providing me the necessary resources to work independently and for her timely advice. I am also thankful to Dr Anok Babu Nagaram who had been with me throughout the phase of this project work and in providing me with relevant expertise in this domain. I would also like to express my gratitude to Dr Antonio Mulone for his valuable technical advice, patience and training me with the lab equipments. I am also grateful to Mr Nils Nordstrom for his valuable suggestions and insights in superalloys.

This work would not have been possible without the support from the Erasmus Mundus META 4.0 Program, special thanks to Aurelie Brayet for her exceptional care during the program. Finally, I extend my appreciation to fellow master students and to all the staff members and friends at Chalmers university (Sweden), Politecnico di Torino (Italy), University of Ljubljana (Slovenia), and Ecole Centrale Lyon ENISE (France), for all the support during my studies.

#### **Abstract**

UDC 620.178.3:543.456:669.245(043.2)

No.: MAG II/1650

#### Characterisation of IN718 Nickel Superalloy Powder Bed Fusion Laser Additive Manufacturing

Saikrishna Suresh Kumar

Keyword:

Additive Manufacturing
Nickel Super-Alloy
Inconel IN718
Scanning Electron Microscopy
Energy-dispersive X-ray spectroscopy

The proposed research investigates additively manufactured Ni-based superalloy Inconel 718 subjected to two distinct post-processing routes: ageing heat treatment and Hot Isostatic Pressing (HIP). A comprehensive characterization was carried out using optical microscopy, SEM imaging, EDS analysis, porosity quantification, grain size measurements, NbC volume fraction analysis, and Vickers hardness testing. The study aims to establish correlations between processing pathways, resulting microstructures, and their influence on mechanical performance, with particular focus on hardness and fatigue behavior. Since the fatigue reliability of LPBF-produced Inconel 718 is strongly limited by microstructural character, the results highlight that lower porosity, moderate grain size, and a controlled NbC distribution contribute to enhanced hardness and fatigue life. Among the examined conditions, sample C3 (Heat treatment and HIP) exhibited the most favorable fatigue performance, while sample B7 (Heat treated) had the lowest fatigue life.

#### Izvleček

UDK 620.178.3:543.456:669.245(043.2)

No.: MAG II/1650

# Karakterizacija mikrostrukture nikljeve superzlitine INCONEL IN718 izdelane z laserskim taljenjem prahu na podlago

Saikrishna Suresh Kumar

Ključne besede:

Dodajalna izdelava Nikeljeva superzlitina Inconel IN718 Skenirna elektronska mikroskopija (SEM) Energijsko disperzna rentgenska spektroskopija (EDS)

Raziskava preučuje dodajalno izdelano superzlitino na osnovi niklja (Inconel 718), ki je bila podvržena dvema različnima postopkoma naknadne obdelave: izločevalnem utrjevanju in vročemu izostatičnemu stiskanju (HIP). Celovita karakterizacija je bila vključevala svetlobno mikroskopijo, SEM in EDS analizo, analizo poroznosti, meritev velikosti zrn, analizo volumskega deleža NbC in merjenje trdote po Vickersu. Namen študije je bil vzpostaviti korelacije med naknadno obdelavo, mikrostrukturami in mehanskimi lastnostnimi, s posebnim poudarkom na trdoti in odpornosti na utrujanje. Odpornost na utrujanje dodajalno izdelanega Inconela 718, izdelanega z laserskim spajanjem prahu na podlago, je močno odvisna od mikrostrukture. Rezultati kažejo, da nižja poroznost, zmerna velikost zrn in enakomerna porazdelitev NbC prispevajo k višji trdoti in odpornosti na utrujanje. Med preučevanimi pogoji je vzorec C3 (toplotno obdelan in HIP) dosegel največjo odpornost na utrujanje, vzorec B7 (toplotno obdelan) pa je imel najnižjo odpornost na utrujanje.

## **Table of contents**

1	Introdu	ction	1
	1.1 Back	ground of the work	1
	1.2 Obje	ctives	2
2	Theoret	ical review	3
	2.1 Supe	ralloys	3
	2.1.1 Ni	ckel-Based Superalloys	5
	2.1.2 St	rengthening Mechanisms in Superalloys	5
	2.1.2.1	Solid Solution Strengthening	5
	2.1.2.2	Precipitation Strengthening	
	2.1.2.3	Dispersion Strengthening.	
		loying Elements and Their Effects on Microstructure and Properties	
	2.1.3.1 2.1.3.2	Chromium (Cr)	
	2.1.3.2	Cobalt (Co)	
	2.1.3.4	Titanium (Ti)	7
	2.1.3.5	Tantalum (Ta) and Niobium (Nb)	
	2.1.3.6 2.1.3.7	Tungsten (W) and Molybdenum (Mo) Carbon (C), Boron (B), Zirconium (Zr),	
	2.1.3.8	Influence of Heat Treatment and Processing Parameters on Microstructure	
	2.1.3.9	Correlation Between Microstructure and Mechanical Properties	9
	2.2 Addi	tive Manufacturing	10
	2.2.1 La	ser Beam Additive Manufacturing	11
	2.2.2 Ef	fects of Powder Characteristics on the LPBF Process	12
	2.3 Post-	Processing techniques	13
	2.4 Princ	ciples of Characterization Techniques	14
		eld Emission Gun Scanning Electron Microscopy (FEG-SEM)	
		Secondary Electrons (SEs)	
	2.4.1.2	Backscattered Electrons (BSEs)	15
	2.4.1.3	Characteristic X-rays and Energy Dispersive X-ray Spectroscopy (EDS)	15
	2.5 Hard	ness Testing	16

3	Materials and Methodology	17
	3.1 Material	18
	3.2 Methodology	19
	3.2.1 Metallography Sample Preparation	
	3.2.1.1 Sectioning and Cutting	
	3.2.1.2 Sample Mounting preparation	
	3.2.2 Etching Technique	
	3.3 Microstructure Characterisation	29
	3.3.1 Microscopy	29
	3.3.2 Field Emission Gun - Scanning Electron Microscopy (FEG-SEM)	30
	3.4 Vickers Hardness Testing	33
	3.5 Fatigue Testing	34
4	Results and Discussion	35
	4.1 Quantitative Analysis & Characterisation	35
	Metal Carbide, MC-type precipitates	35
	Grain size and anisotropy	38
	Role of Grain Boundary Pinning	45
	4.1 Fatigue Life Performance	48
5	Conclusion	51
6	Limitations and future work	52
D'	:h!:	<b>5</b> 2
<b>B</b> ]	ibliography	53

# **Table of figures**

Figure 2.1 Illustration of material usage in a jet engine (Courtesy: Rolls Royce) [24]	4
Figure 2.2 Evolution of the high temperature capability of the superalloy over a 60 year positive their emergence in the 1940s [24]	
Figure 2.3 Timeline sequence development of Additive manufacturing technology [2]	10
Figure 2.4: Vickers hardness Measurement according to ASTM E84 standard [18]	
Figure 3.1 Fatigue life of all the four samples	
Figure 3.2 Metallography preparation lab	21
Figure 3.3 Sequence of metallography procedure	21
Figure 3.4 Cutting machine and samples cut in XYand XZ axis	22
Figure 3.5: Cutting Section Plane	
Figure 3.6 Mounting Machine	
Figure 3.7 Mounting preparation	
Figure 3.8 Grinding machine	
Figure 3.9 Samples after polished and cleaned	
Figure 3.10 (a) Etchant preparation and (b) sample being etched	
Figure 3.11 (a) Picture of an optical microscope device (b) Image captured using the mic	roscope.
Figure 3.12: EDS Spectrum analysis of three particles marked from figure (a)	
Figure 3.13 (a) Picture of a SEM machine and (b) EDX software window	
Figure 3.14 (a) Hardness Testing Device, (b) Microscopic Image of the indentation	
Figure 3.15 Specimens with fillets for fatigue tests	
Figure 4.1 EDX mapping of specimen sample C3 post processed	36
Figure 4.2: EDS analysis confirming NbC particle	
Figure 4.3 Specimen B7 at EDX analysis	
Figure 4.4: NbC is identified from the spectrum for B7	
Figure 4.5: Grain size across orientation plane (Z and XY)	
Figure 4.6: B7 (HeatTreated) micrograph along a) XZ and b) XY plane	
Figure 4.7: B10 micrograph along a) XZ and b) XY plane	
Figure 4.8: C3 micrograph along a) XZ and b) XY plane	
Figure 4.9: C12 micrograph along a) XZ and b) XY plane	43
Figure 4.10: Grain-size anisotropy ratio, dashed line denotes isotropy	
Figure 4.11: NbC (relative to C3) vs average grain size (linear trendline shown)	
Figure 4.12: Vickers Hardness across four samples	
Figure 4.13: Average grain size vs average hardness (linear trendline shown)	
Figure 4.14: Fatigue life at 700 MPa (log scale)	
Figure 4.15: Average hardness vs fatigue life (log scale; trendline fit in log-space)	

## **List of Tables**

Table 2.1: Mechanical property and microstructural feature correlation	10
Table 3.1 : Powder Chemical Composition wt-% [54]	18
Table 3.2 Fatigue performance and heat treatment of samples.	34
Table 4.1: Measured NbC precipitate volume fractions and relative values to sample C3	38
Table 4.2: Measured grain sizes.	38
Table 4.3: Summary of microstructural and Hardness metrics.	46
Table 4.4: Measured porosity (%) and corresponding relative density	48

# 1 Introduction

#### 1.1 Background of the work

Additive manufacturing (AM) has become an integral part of modern manufacturing and engineering, enabling the design and fabrication of complex shaped, high performance parts with unprecedented geometrical freedom and near net-shape precision. Among the various AM techniques, Laser Powder Bed Fusion (LPBF) has gained widespread attention for its precision and suitability for processing advanced metallic alloys, especially nickel-based superalloys such as Inconel 718 (IN718) owing to its weldability characteristics.

Inconel 718® is renowned for its exceptional strength, corrosion resistance, and stability at elevated temperatures, making it a primary candidate for aerospace, power generation, and marine applications. These properties are achieved through a complex precipitation hardening mechanism involving nanoscale phases like  $\gamma'$  (Ni<sub>3</sub>(Al,Ti)) and  $\gamma''$  (Ni<sub>3</sub>Nb), embedded in an austenite  $\gamma$  matrix. However, the rapid solidification, high thermal gradients, and repeated heating cycles in LPBF processes often result in undesirable features such as porosity, elemental segregation, anisotropic grain growth, and the formation of detrimental phases like Laves and  $\delta$ -phase.

To address these microstructural issues, post-processing treatments especially Hot Isostatic Pressing (HIP) and ageing heat treatments are employed to densify the structure and optimize phase composition. As the process are non-standardized and unoptimized there is a considerable variability in mechanical performance, particularly fatigue strength in this research work. Understanding the microstructural differences of this variability is critical for ensuring the reliability of LPBF-fabricated IN718 components.

This thesis report focuses on the microstructural characterization and phase analysis of four IN718 samples manufactured by LPBF, each subjected to different post-processing routes. Through systematic imaging and image analysis techniques (SEM, EDS, and Weka Segmentation), the study seeks to explore the root causes of mechanical performance variation and propose microstructural indicators that could predict fatigue behaviour in IN718 superalloy.

#### 1.2 Objectives

The core aim of this research work is to systematically investigate microstructural features arising from LPBF samples and its heat treatment influence of the mechanical behaviour primarily fatigue life of Inconel 718 superalloy. The work addresses the following main objectives:

- To conduct a comprehensive review of the scientific literature on LPBF processing of IN718, microstructural evolution and the use of specialized equipment, and post-processing strategies in influencing defect formation and phase, thereby establishing a theoretical foundation for the experimental analysis.
- To characterize and compare the microstructure of four additive manufactured Inconel 718 samples each subjected of distinct post-processing treatments (ageing heat treatment and HIP), using scanning electron microscopy (SEM), energy-dispersive X-ray spectroscopy (EDS), porosity quantification via image analysis, and grain size measurements, in order to identify anomalies such as residual pores, deleterious phases, and grain morphology.
- To analyse the percentage distribution and chemistry of critical phases (Laves,  $\delta$ ,  $\gamma'/\gamma''$ , non-metallic inclusions such as carbides and oxides) through SEM-EDS imaging and using tools such as ImageJ, MATLAB, and Trainable Weka Segmentation plug-ins.
- **To understand** the variation in fatigue life behaviour of the processed samples by comparing experimental outcomes and test results against theoretical literature findings, highlighting how varying post-processing mitigates defects and enhances properties.

# 2 Theoretical review

#### 2.1 Superalloys

A specific group of material alloys designed to retain exceptional strength and other properties across a wide temperature range, from ambient to elevated and, in some cases, cryogenic conditions. They were specially developed to meet the growing industries needs to build advanced systems with optimal material strength to property ratio. One of them is based on Nickel alloy falls into this large category of materials which was developed in the mid-20<sup>th</sup> century and popularity rise due to high melting point property of Nickel (1453 °C) and adequate corrosion resistance with ability to improve strength by dissolving few known elements. [3]

Under specific compositional and heat-treatment conditions, a stable MC-type carbide phase may form. Additionally, laves phases can appear in nickel-based superalloys, typically after prolonged exposure to high temperatures. [3] One of the earliest significant nickel-based superalloys was Nimonic 75, an evolution of Nichrome alloys originally used in furnace resistance wiring. Nimonic 75 consists primarily of a chromium-nickel solid solution with dispersed MC-type carbides. Around the same period, a comparable American alloy, Inconel (like the modern Inconel 600), was developed. These alloys offered superior high-temperature strength and oxidation resistance compared to stainless steels. Subsequent advancements in superalloy development involved adding aluminium and titanium to form Ni-based precipitates. [1]

Development were made further to improve the solid solution strengthening by adding refractory metals and an increase in Aluminium and Titanium content for  $\gamma'$  precipitates within the limits of forging capabilities and further additions with the improvement in investment casting technology.

In applications where significant resistance to loading under static, fatigue and creep conditions is required, the nickel-base superalloys are a solution for high temperature application parts as in aero engines, however, in the combustor and turbine arrangements, the nickel-based superalloys are used almost exclusively for temperatures at or exceeding 700 °C. Other Superalloys are also used in the final (high-pressure) stages of the compressor, figure 2.1. [2]

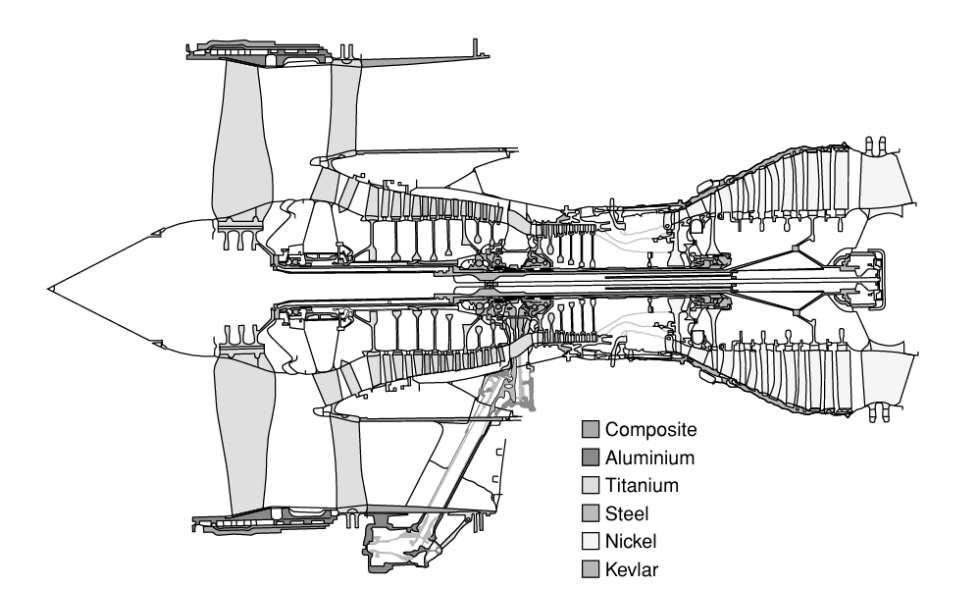


Figure 2.1 Illustration of material usage in a jet engine (Courtesy: Rolls Royce) [1]

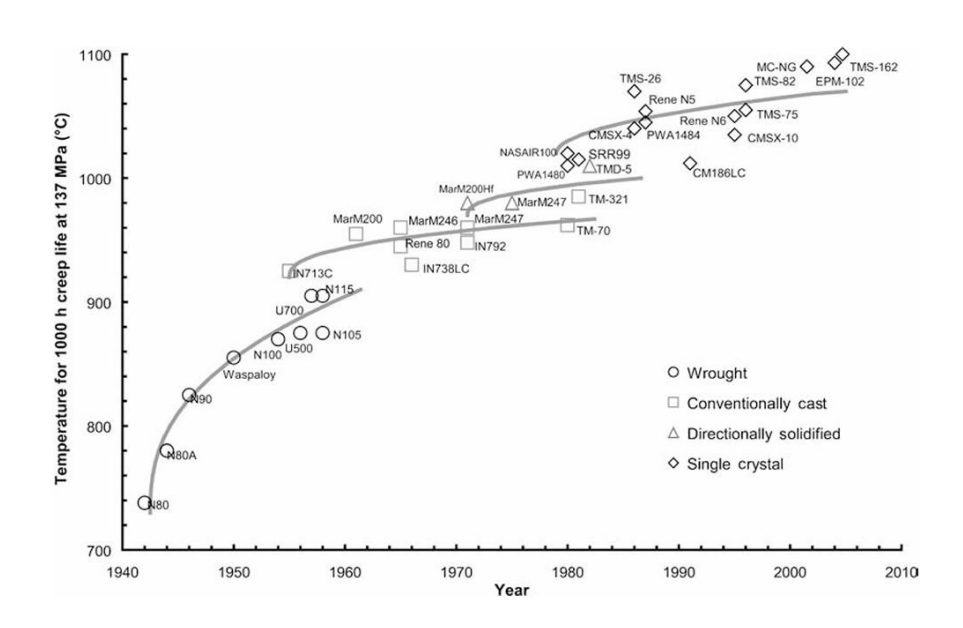


Figure 2.2 Evolution of the high temperature capability of the superalloy over a 60 year period since their emergence in the  $1940s\ [1]$ 

#### 2.1.1 Nickel-Based Superalloys

Nickel-based superalloys are characterized by a two-phase microstructure comprising a gamma ( $\gamma$ ) matrix, which is a face-centered cubic (FCC) solid solution, and gamma-prime ( $\gamma$ ') precipitates, ordered intermetallic compounds typically of the form Ni<sub>3</sub>(Al,Ti). The  $\gamma$ ' phase is primarily responsible for the alloys' high-temperature strength and creep resistance, owing to its ordered L1<sub>2</sub> structure and coherent interface with the  $\gamma$  matrix. The composition of these alloys includes various alloying elements to enhance specific properties:

- Aluminium (Al) and Titanium (Ti): Essential for forming the  $\gamma'$  phase, which contributes to precipitation strengthening.
- Chromium (Cr): Enhances oxidation and corrosion resistance.
- Cobalt (Co): Stabilizes the  $\gamma$  matrix and improves high-temperature properties.
- Molybdenum (Mo) and Tungsten (W): Provide solid solution strengthening.
- Other Elements: Tantalum (Ta), niobium (Nb), rhenium (Re), and others are added to tailor specific properties, such as creep resistance or phase stability.

Common nickel-based superalloys figure 2.2 include Inconel 718, Inconel 625, and CMSX-4, each optimized for specific applications. For instance, Inconel 718 is widely used in aerospace due to its balance of strength and weldability, while CMSX-4 is preferred for single-crystal turbine blades due to its superior creep resistance.[1]

#### 2.1.2 Strengthening Mechanisms in Superalloys

Nickel-based superalloys, often incorporating cobalt (Co) or a combination of nickel (Ni) and iron (Fe) as base elements, possess a facecentered cubic (FCC) crystal structure, referred to as the gamma ( $\gamma$ ) phase. This phase provides a robust and ductile foundation for alloying, characterized by stability up to the solidus temperature, high solubility for alloying elements, and the formation of protective oxides when combined with chromium (Cr) and aluminium (Al). These attributes enable multiple strengthening mechanisms, including solid solution strengthening, precipitation strengthening, and dispersion strengthening. Grain size strengthening, however, is less effective in superalloys due to the high-temperature service conditions, where grain boundary strengthening diminishes [8].

#### 2.1.2.1 Solid Solution Strengthening

The inherent yield strength of pure nickel is approximately 110 MPa at ambient temperature, necessitating alloying to enhance mechanical properties. Solid solution strengthening is achieved by incorporating elements with significant atomic radius differences relative to the base elements (Ni, Fe, or Co). Elements such as aluminium (Al), tungsten (W), molybdenum (Mo), and chromium (Cr) are particularly effective, with their large atomic sizes inducing lattice distortions that impede dislocation motion. This mechanism is highly effective at elevated temperatures, making it a cornerstone of superalloy performance. Additionally, alloys designed for oxidation and corrosion resistance often rely on solid solution strengthening elements to enhance mechanical properties. However, elements like Mo and W, while potent for strengthening, can promote the formation of deleterious topologically close-packed (TCP) phases during prolonged high-temperature exposure and may adversely affect hot corrosion resistance [8].

#### 2.1.2.2 Precipitation Strengthening

The exceptional high-temperature strength and creep resistance of modern nickel-based superalloys are primarily attributed to the presence of high volume fractions of strengthening precipitates, such as the gamma-prime ( $\gamma'$ ) phase in Ni-based alloys and the gamma-double-prime ( $\gamma''$ ) phase in Ni-Fe-based alloys. These thermodynamically stable intermetallic phases are precipitated from a supersaturated solid solution through controlled ageing heat treatments. The  $\gamma'$  phase, with a nominal composition of A<sub>3</sub>B (where A is Ni or Co, and B is Al, Ti, Ta, or Nb), adopts an ordered L1<sub>2</sub> crystal structure that is coherent with the  $\gamma$  matrix. The strengthening effect arises from the increased energy required for dislocations to traverse the ordered precipitate structure, influenced by factors such as precipitate size, volume fraction, coherency strains (due to lattice parameter mismatches between  $\gamma$  and  $\gamma'$ ), and anti-phase boundary (APB) energy. The effectiveness of precipitation strengthening is limited by the solvus temperature of the precipitates, above which they dissolve into the matrix [8,9].

#### 2.1.2.3 Dispersion Strengthening

Dispersion strengthening, facilitated by carbides and oxides, is another critical mechanism in superalloys. Incoherent dispersoids, such as carbides, are typically located at grain boundaries in cast and wrought Ni-based superalloys, where they stabilize grain boundaries and enhance creep resistance and strength, particularly in discrete or blocky morphologies. Intragranular carbides can also act as barriers to dislocation motion, similar to precipitates. Oxide dispersion strengthened (ODS) superalloys, often manufactured via powder metallurgy (PM) processes, incorporate approximately 1 wt.% of nanoscale oxides, such as yttria, which remain stable at temperatures exceeding the alloy's melting point. This stability contributes to exceptional creep resistance, positioning ODS superalloys as a distinct class of materials for extreme high-temperature applications [8,9].

# 2.1.3 Alloying Elements and Their Effects on Microstructure and Properties

Nickel-based superalloys are among the most compositionally complex alloys, frequently incorporating over ten alloying elements to achieve tailored properties for specific applications. The influence of each element is multifaceted, modulated by interactions with other alloying elements, the alloy's manufacturing process, and its intended service environment. This section elucidates the primary roles of key alloying elements in polycrystalline Ni-based superalloys, focusing on their contributions to microstructure and mechanical properties.

#### **2.1.3.1** Chromium (Cr)

Chromium is a ubiquitous alloying element in superalloys, typically present in significant quantities. It serves as a potent solid solution strengthened, enhancing the alloy's mechanical properties by inducing lattice distortions. Additionally, Cr promotes the rapid formation of chromia (Cr<sub>2</sub>O<sub>3</sub>), a protective oxide layer that provides robust resistance to hot corrosion. However, excessive Cr can lead to the formation of deleterious topologically close-packed (TCP) phases during prolonged high-temperature exposure, which compromise alloy strength and ductility [8,9].

#### **2.1.3.2 Aluminium (Al)**

Aluminium, added in smaller quantities than Cr, plays a critical role in both surface oxide stability and mechanical performance. In the aged condition, Al forms the gamma-prime ( $\gamma$ ') phase, an ordered intermetallic that drives precipitation strengthening. In solid solution, Al contributes to solid solution strengthening. Furthermore, Al facilitates the formation of alumina (Al<sub>2</sub>O<sub>3</sub>), a highly stable oxide at elevated temperatures, offering superior oxidation resistance compared to chromia. To favour alumina formation over chromia, a Cr-to-Al ratio of 4 or less is typically required [8,9].

#### 2.1.3.3 Cobalt (Co)

Cobalt is frequently added in substantial amounts to Ni-based superalloys, as it elevates the alloy's solidus temperature, enhancing high-temperature stability. Additionally, Co increases the volume fraction and stability of the  $\gamma'$  phase, thereby augmenting precipitation strengthening and overall alloy strength [8,9].

#### **2.1.3.4** Titanium (Ti)

Similar to aluminium, titanium enhances the volume fraction of the  $\gamma'$  phase and raises its solvus temperature, contributing to precipitation strengthening. Ti also increases the antiphase boundary (APB) energy of the  $\gamma'$  phase, further enhancing strength. As a strong carbide former, Ti segregates with carbon to the liquid phase during solidification, forming MX-type carbides in interdendritic regions upon cooling, which can influence microstructural stability and creep resistance [9].

#### 2.1.3.5 Tantalum (Ta) and Niobium (Nb)

Tantalum and niobium play comparable roles in nickel-based superalloys, primarily enhancing the volume fraction of the gamma-prime ( $\gamma$ ') phase, which contributes to precipitation strengthening. Despite their significant lattice misfit with the  $\gamma$  matrix, their solid solution strengthening effect is limited, as they predominantly partition to the  $\gamma$ ' phase or are incorporated into stable MX-type carbides. Due to tantalum's high density and cost, niobium is often preferred in cost-sensitive applications, offering similar benefits to  $\gamma$ ' phase stability and strengthening at a lower economic and weight penalty [9].

#### 2.1.3.6 Tungsten (W) and Molybdenum (Mo)

Tungsten and molybdenum, both heavy refractory elements, are potent solid solution strengtheners in Ni-based superalloys due to their large atomic sizes, which induce significant lattice distortions. These elements reduce overall diffusivity in the  $\gamma$  matrix, enhancing the stability of carbides and  $\gamma'$  phases, thereby mitigating creep deformation mechanisms. Additionally, W and Mo increase the alloy's solidus temperature and the solvus temperature of the  $\gamma'$  phase, further improving high-temperature performance. However, their oxides are unstable, leading to poor hot corrosion resistance. Similar to chromium, excessive W and Mo can promote the formation of deleterious topologically close-packed (TCP) phases during prolonged high-temperature exposure, which may compromise mechanical properties [8,9].

#### 2.1.3.7 Carbon (C), Boron (B), Zirconium (Zr),

Minor alloying elements such as carbon, boron, zirconium, and hafnium are incorporated in small quantities but exert significant influence on the properties of polycrystalline Ni-based superalloys, primarily through their effects at grain boundaries due to their limited solubility in the  $\gamma$  matrix.

#### 2.1.3.7.1 Carbon (C)

Carbon is primarily added to form carbides, which strengthen grain boundaries when present in appropriate morphologies and quantities. During liquid processing, carbon acts as a deoxidizing and de-sulfurizing agent, enhancing the fluidity of the molten metal. However, carbon segregates strongly to the last-to-solidify liquid during casting, which can impair weldability in many superalloys [8,9].

#### 2.1.3.7.2 Boron (B)

Boron is added in trace amounts (typically <0.1 wt.%) and significantly enhances creep strength and ductility. Its primary mechanism is believed to involve the suppression of grain boundary diffusion processes that lead to creep failure. At low concentrations, boron exists in elemental form at grain boundaries, while at higher levels, it forms borides with elements such as W, Mo, and Cr. Boron also inhibits carbide coarsening and grain growth, contributing to microstructural stability. However, excessive boron can reduce weldability and significantly lower the incipient melting temperature of superalloys [8,9].

#### 2.1.3.7.3 Zirconium (Zr)

Zirconium is traditionally considered beneficial for improving creep properties by preventing the agglomeration of grain boundary carbides, thereby reducing the formation of microcracks. However, recent advancements have led to high creep strength alloys without Zr, casting doubt on its necessity. Like boron, Zr acts as a melting point depressant and can synergistically interact with B, further exacerbating weldability challenges [8,9].

# 2.1.3.8 Influence of Heat Treatment and Processing Parameters on Microstructure

The microstructure of nickel-based superalloys is highly sensitive to heat treatment and processing parameters, which are critical for optimizing their performance. Heat treatment typically involves two main steps:

- 1. **Solution Treatment**: The alloy is heated to a high temperature (e.g., 980-1330°C) to dissolve  $\gamma'$  precipitates into the  $\gamma$  matrix, followed by rapid cooling to create a supersaturated solid solution. The temperature and cooling rate determine the grain size and the extent of  $\gamma'$  dissolution. For example, super solvus treatments (above the  $\gamma'$  solvus temperature) result in coarser grains due to the absence of  $\gamma'$  pinning effects, while sub-solvus treatments maintain finer grains.[11]
- 2. **Ageing**: Subsequent heating at lower temperatures (e.g.,  $620\text{-}720^{\circ}\text{C}$ ) allows controlled precipitation of  $\gamma'$  particles. A two-step ageing process can produce a bimodal distribution of  $\gamma'$  precipitates coarser particles from the first step and finer secondary particles from the second optimizing both strength and ductility. [10]

#### 2.1.3.9 Correlation Between Microstructure and Mechanical Properties

The mechanical properties of nickel-based superalloys are intricately linked to their microstructure, particularly the size, shape, volume fraction, and distribution of  $\gamma'$  precipitates:

- Strength: The volume fraction and size of  $\gamma'$  precipitates significantly influence yield strength. Finer precipitates (e.g., 80-190 nm) increase strength through particle hardening mechanisms, as dislocations must bypass or cut through these precipitates. For example, a higher volume fraction of  $\gamma'$  in alloys like CMSX-4 (a nickel-based single-crystal superalloy) enhances tensile strength compared to Inconel 718.
- Creep Resistance: The stability of the  $\gamma'$  phase at high temperatures and its resistance to coarsening or rafting under stress are critical for creep performance. Rafting, where  $\gamma'$  precipitates elongate under tensile stress, can enhance creep resistance at low stresses by impeding dislocation climb but may be detrimental at high stresses due to easier dislocation cutting.
- **Ductility**: The distribution of  $\gamma'$  and other phases, such as carbides or Laves phases, affects ductility. Excessive  $\gamma'$  can lead to brittleness, while a balanced microstructure ensures adequate ductility. In AM-processed superalloys, the presence of defects like porosity or microcracks can further influence ductility.
- Fatigue resistance in nickel-based superalloys depends on both precipitate morphology and defect contents. Fine and uniformly distributed γ'/γ" precipitates enhance fatigue life by impeding dislocation motion, reducing localized plastic deformation, and delaying crack initiation under cyclic loading [1], [6]. In contrast, coarse precipitates or excessive δ-phase precipitation at grain boundaries may act as crack initiation sites, accelerating fatigue failure

Table 2.1: Mechanical property and microstructural feature correlation

Microstructural Feature	Mechanical Property Impact	Example
Fine γ' precipitates	llincreaced weld strength	CMSX-4 with $\sim$ 128 nm $\gamma'$ particles
High γ' volume fraction	Enhanced creep resistance	Single-crystal alloys like CMSX- 4
Columnar grains (AM)	Anisotropic strength/ductility	EBM Inconel 718

#### 2.2 Additive Manufacturing

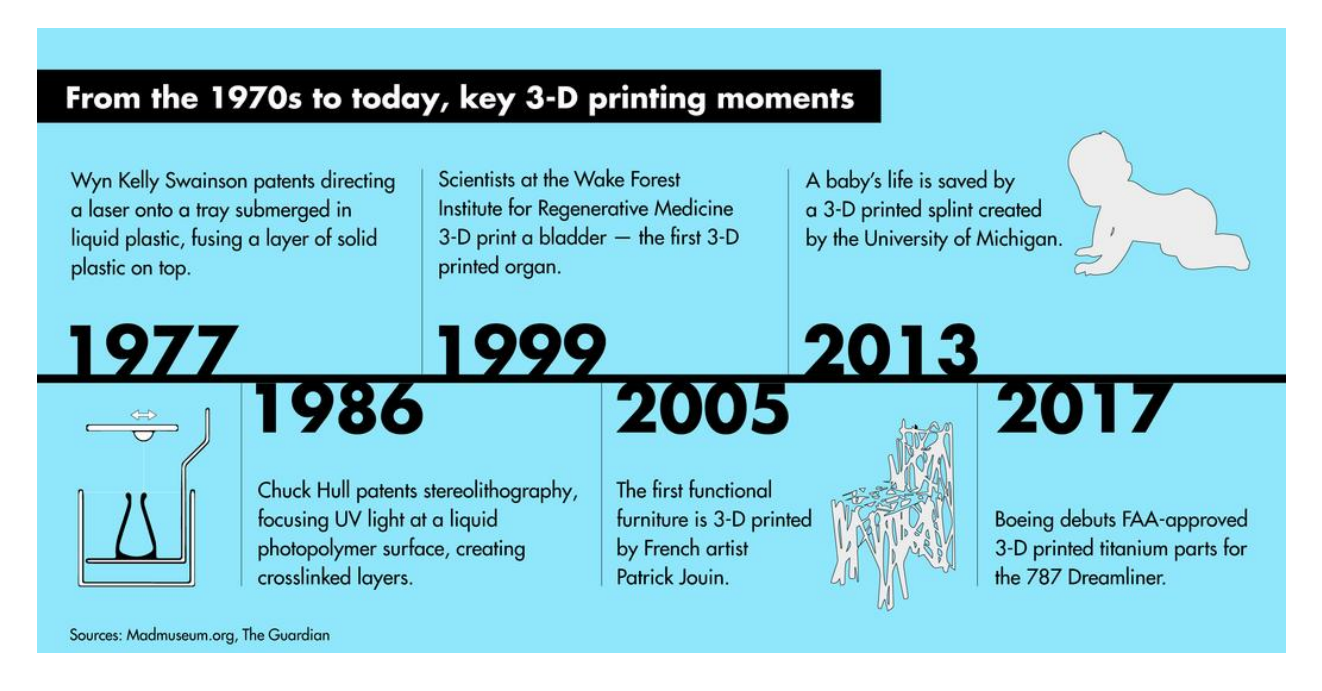


Figure 2.3 Timeline sequence development of Additive manufacturing technology [2]

Additive manufacturing (AM) is an advanced fabrication process that constructs three-dimensional objects through the sequential addition of material layers. In contrast to subtractive manufacturing, which involves removing material from a solid block to achieve the desired geometry, AM builds components incrementally until the final form is realized.

Broadly, additive manufacturing encompasses any technique that involves the progressive addition of material, such as molding processes.

However, in contemporary usage, the term is predominantly associated with 3D printing technologies, which enable precise, layer-by-layer fabrication of complex geometries along with recent advancements almost reducing post process treatments related to surface finish.

By the early 2000s, additive manufacturing was being used to create functional prototypes. More recently, companies like Boeing and General Electric have made additive manufacturing an integral part of their business processes. Compared to traditional manufacturing which is still faster and less expensive for batch production but has significant initial investment. The smaller the layer size, which improves the quality but comes with the slower pace of manufacturing. While the initial steps are cheaper and faster when made with additive manufacturing, in the long run, printing out every unit would take longer. Significant achievement is the ability to print complex and unique geometry and functionally graded material combining different materials of different properties printed as one component. [2]

#### 2.2.1 Laser Beam Additive Manufacturing

**Laser** Beam Additive Manufacturing (LBAM), such as Selective Laser Melting (SLM) or Direct Metal Laser Sintering (DMLS), is a **Powder Bed Fusion process** that builds parts layer by layer by selectively melting metal powder with a high-power laser, typically an ytterbium fiber laser.

A typical laser additive manufacturing system includes a laser, a scanning galvanometer, a forming cylinder, and a computer control system.

#### The process involves:

- 1. **Powder Spreading**: A thin layer of metal powder (20-100 μm) is spread over a build platform using a roller or blade.
- 2. **Laser Melting**: A laser beam scans and melts the powder according to a 2D slice of a 3D computer-aided design (CAD) model, fusing it to the previous layer.
- 3. **Platform Lowering**: The build platform is lowered, and a new layer of powder is spread, repeating the process until the part is complete.
- 4. **Controlled Environment Chamber**: The process occurs in an inert gas atmosphere (argon or nitrogen) to minimize oxidation and other contamination inside the chamber.

Laser Beam Additive manufacturing offers design flexibility, enabling the production of complex geometries that are challenging with traditional manufacturing methods. It is particularly suited for nickel-based superalloys due to their high-temperature applications in aerospace and energy sectors.

#### 2.2.2 Effects of Powder Characteristics on the LPBF Process.

The process parameters of laser powder bed fusion (LPBF), combined with the energy absorption characteristics of the powder under laser irradiation, determine the volumetric energy density available for heating and melting the powder feedstock. Powder absorptance, defined as the ratio of absorbed energy flux to the incident energy flux, is influenced not only by the physical and chemical properties of the powder material but also by its granulometry and apparent density. Compared to the bulk counterparts, powder materials exhibit significantly higher absorptance, regardless of the laser type employed. For instance, the absorptance values for bulk materials are approximately 0.3 for titanium (ATi bulk), 0.36 for iron (AFe bulk), and 0.02 for copper (ACu bulk), whereas the corresponding powder forms demonstrate elevated absorptance values of 0.77 for titanium (ATi powder), 0.64 for iron (AFe powder), and 0.59 for copper (ACu powder) at a wavelength of 1.06 µm.[6]

Powder size and powder distribution can influence the LPBF process parameters. Powders with a narrow range of particle size exhibit better flow and produce parts with improved qualities such as surface finish, hardness, and mechanical properties [3]

The inert gas flow delivery across the build platform in the LPBF process, as indicated by Ferrar et al. [4] significantly influences the quality and reproducibility of components across the build area. The porosity density of LPBF built parts can be enhanced when the gas flow is highly uniform [4]. Inert gases also provides a secondary function to remove any process by-products such as spatter, condensate, and welding fumes from the path of the laser as they may potentially affect the laser beam properties such as energy, spot diameter and intensity profile during the process[8]. Masmoudi et al. asserted that by adjusting shielding gas pressure, controls the volume of the evaporated material. The authors mention that relatively high-pressure argon shielding gas narrows the evaporated material into a smaller volume leading to improvement in density.

#### 2.3 Post-Processing techniques

The microstructure of superalloys produced via laser powder bed fusion (LPBF) differs significantly from that of conventionally manufactured counterparts, necessitating a reevaluation or redesign of traditional solution and ageing heat treatments. Conventional heat treatments, optimized for cast or wrought microstructures, may not be directly applicable to the unique, often finer, and more anisotropic microstructures resulting from LPBF. To address defects inherent in LPBF-processed superalloys, post-processing techniques such as hot isostatic pressing (HIP) are frequently employed to enhance material density and integrity.

Therefore, post-processing is critical for optimizing the microstructure and mechanical properties of AM-fabricated superalloys. Common techniques include:

- **Hot Isostatic Pressing (HIP)**: Applies high pressure and temperature to close internal pores, achieving near-full density (e.g., 99.5% in EBM Haynes 282).
- Heat Treatment: Solution treatment (e.g., 980-1100°C) dissolves unwanted phases (e.g., Laves or δ phases in Inconel 625) and promotes uniform γ' precipitation. Ageing (e.g., 720°C and 620°C) further refines the γ' morphology.

For instance, a combined HIP and heat treatment cycle can homogenize the microstructure, reduce anisotropy, and enhance mechanical properties like tensile strength and ductility.[40]

Different alloy systems necessitate tailored heat treatments. However, components produced through Laser Powder Bed Fusion (LPBF) typically require at least a stress relief heat treatment prior to their removal from the building platform. This procedure is essential to prevent deformation of the part due to the high residual stress inherent in the as-built condition once the constraining effects of the building platform are eliminated. Additional heat treatments, such as homogenization, solution treatment, and aging, may also be required based on the specific demands of the alloy system or the intended application.

HIP is frequently employed in the production of high-performance LPBF components, particularly in the medical and aerospace sectors, to mitigate residual defects in crack-susceptible alloys, processed via LPBF. The HIP process involves subjecting components to elevated temperatures while simultaneously applying high gas pressure (100 MPa or more) uniformly from all directions. This method induces small-scale plastic deformation, effectively closing voids and pores. Furthermore, HIP can be integrated with other heat treatment processes to streamline the overall manufacturing sequence.

The distinctive microstructure of LPBF-manufactured components indicates that conventional heat treatments designed for cast or wrought alloys may not be appropriate for LPBF alloys. Consequently, it may be necessary to develop new HIP or heat treatment protocols to achieve the desired material properties in LPBF components.

Studies indicated that HIP effectively heals internal microcracks and porosity, improving mechanical properties. However, its efficacy is limited for surface-connected cracks or large argon-filled pores.

Ferrar et al. demonstrated that microcracks up to 6 µm in width in IN738LC could be successfully healed using HIP, underscoring its potential and limitations [4].

These findings highlight the potential to optimize post-processing strategies for LPBF superalloys, achieving mechanical properties comparable to those of cast and wrought materials while preserving the geometric flexibility and design advantages offered by additive manufacturing.

#### 2.4 Principles of Characterization Techniques

Characterization techniques are essential for analysing the microstructure and properties of superalloys, providing insights into the effects of processing and heat treatment

- Scanning Electron Microscopy (SEM): Uses a focused electron beam to produce high-resolution images of surface morphology and microstructure. In superalloys, SEM is used to observe precipitate size, shape, and distribution, as well as defects like cracks or porosity.
- Energy Dispersive Spectroscopy (EDS): Coupled with SEM, EDS analyses the elemental composition of specific regions, enabling phase identification and mapping of alloying elements (e.g., Ni, Cr, Al).
- Optical Microscopy: Provides lower-magnification images for observing larger features, such as grain structures, inclusions, or macro-defects. It is useful for assessing grain size and orientation in AM parts.
- Vickers Hardness Testing: Measures material hardness by indenting the surface with a diamond pyramid and measuring the indentation size. Hardness correlates with strength and can indicate the effectiveness of heat treatments.

These techniques collectively enable a comprehensive understanding of the process-structure-property relationships in nickel-based superalloys, guiding the optimization of manufacturing and post-processing strategies. Detailed theoretical understanding has been explained further in subsections.

# 2.4.1 Field Emission Gun Scanning Electron Microscopy (FEG-SEM)

Scanning electron microscopy (SEM) is a versatile analytical technique capable of providing diverse information based on user requirements. As implied by its name, SEM employs a focused electron beam to scan the surface of a specimen, generating various signals through interactions with the sample. These signals include secondary electrons (SEs), backscattered electrons (BSEs), characteristic X-rays, and Auger electrons, which are detected by specialized detectors attached within the machine to yield valuable insights into the material's properties across layers in micron and nano level range. [12]

#### 2.4.1.1 Secondary Electrons (SEs)

Secondary electrons, originating from atoms in the near-surface region of the specimen, are produced through inelastic interactions between the primary electron beam and surface atoms. The interaction volume of SE is a smaller field compared to BSE and X-rays. Evenif the electron beam may penetrate to micrometer depths, only SEs generated within approximately 10 nm of the surface can escape and be detected. This shallow escape depth makes SEs ideal for high-resolution topographic imaging, typically achieving resolutions of 10 nm, enabling detailed visualization of surface morphology. [13]

#### 2.4.1.2 Backscattered Electrons (BSEs)

In contrast to SEs, backscattered electrons are primary electrons that undergo elastic scattering with sample's atoms, retaining their initial energy. The interaction volume of BSEs is larger, extending to several tens of nanometers, resulting in lower topographic resolution compared to SEs. However, BSEs provide compositional contrast, as heavier atoms with higher atomic numbers scatter electrons more effectively, producing stronger signals. This characteristic enables BSE imaging to differentiate phases and map compositional variations within the specimen. [13]

# 2.4.1.3 Characteristic X-rays and Energy Dispersive X-ray Spectroscopy (EDS)

In addition to SEs and BSEs, the interaction of the electron beam with the specimen can eject inner-shell electrons, creating vacancies that are filled by outer-shell electrons. This process releases characteristic X-rays, whose energies are unique to the atomic transitions involved, enabling identification of the specimen's chemical composition. Energy dispersive X-ray spectroscopy (EDS), integrated into SEM systems, leverages these X-rays to provide quantitative elemental analysis. The spatial resolution of EDS, influenced by sample composition and beam energy, is typically on the order of 1µm. [13][22]

#### 2.5 Hardness Testing

The hardness of a material is a measure of resistance to local plastic deformation and hence directly proportional to its strength. Typically, a diamond-based indenter with known standardized geometry is pressed with a given force on the sample's surface along its normal direction for a specified time. Afterwards the area of the very top section of the indentation obtained on the sample's surface is measured using an optical method. The hardness is then defined as the ratio between the force and the measured area. A highly polished square-based pyramidal diamond indenter with an angle a of 136 ° between its faces is used. Such an indenter and the produced indentation is schematically shown in Figure 2.4.

Vickers hardness number HV number is an expression of hardness of the surface obtained by dividing the force applied to a Vickers indenter by the surface area of the permanent impression made by the indenter. Vickers indenter, a square-based, pyramidal-shaped diamond indenter with face angles of 136° 00'.

This test uses an indentation hardness test using a calibrated machine to force a pointed, square-based, pyramidal diamond indenter having specified face angles, under a predetermined force, into the surface of the material under test and to measure the surface-projected diagonals of the resulting impression after removal of the force. The Vickers indenter creates a square impression from which two surface-projected diagonal lengths are measured. Vickers hardness is calculated from the ratio of the applied force to the area of contact of the four faces of the undeformed indenter. [12]

The applied force can vary from 0.098 N to 980.7 N. Test is a micro hardness test if the force is not larger than 0.980 N while it is a macro hardness test if the force is larger than 0.980 N. Generally harder materials like Nickel superalloy undergoes macrohardness test to evaluate its overall property. The used force is generally indicated in the Vickers hardness, as in the present study a force of 98.07 N, equivalent to a load of 10 kg is chosen, the hardness is called HV 10.

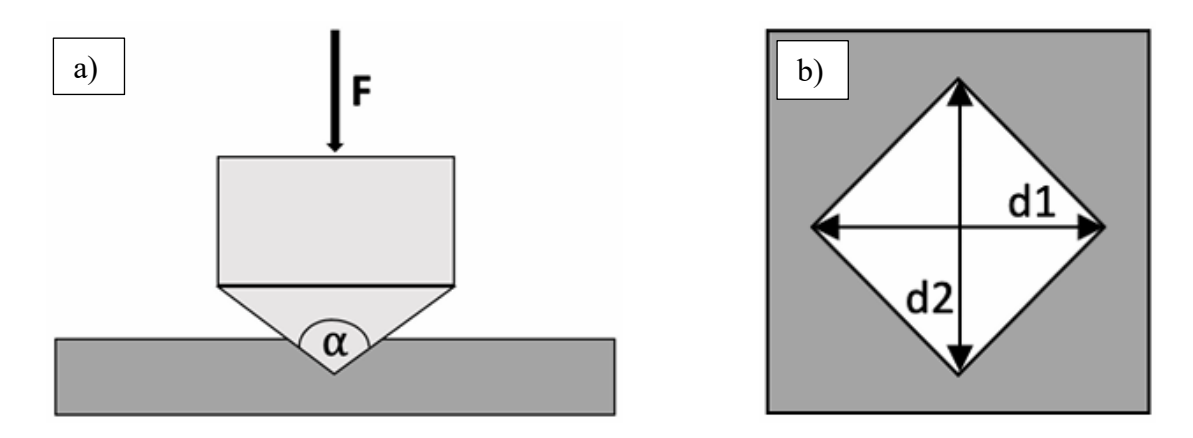


Figure 2.4: Vickers hardness Measurement according to ASTM E84 standard [18]

# 3 Materials and Methodology

The study investigates the relationship between post-processing treatment, microstructural features, and mechanical performance of LPBF Inconel 718 parts. The experiments were structured to:

- Compare porosity, grain size, and secondary phase formation across four samples.
- Relate these features to Vickers hardness and fatigue life as a mechanical property.
- Establish process-structure-property correlations to explain variations in fatigue performance indirectly.

This methodology enables identification of microstructural indicators (e.g., phase fraction, pore distribution) that may predict mechanical strength and reliability in AM-fabricated Inconel 718 components.

Much of the research has been directed towards a fundamental understanding of the effects of the various constituents and precipitates as they regulate mechanical properties

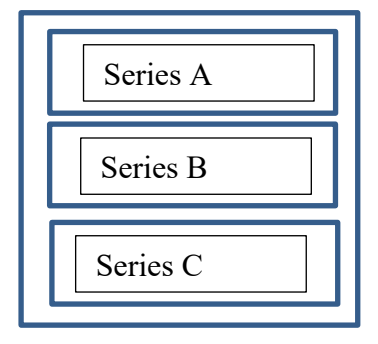


Fig (i) A pictorial representation of specimen samples printed in the LPBF machine

#### 3.1 Material

The primary material used in this study is Nickel super-alloy **Inconel 718 (IN718®)**, a precipitation hardened nickel-based superalloy widely used in aerospace and energy sectors for its high strength, oxidation and corrosion resistance, and superior performance at elevated temperatures from cryogenic to up to 700 °C. At room temperature the fatigue limit is found to be at 690 MPa (100 ksi) for unnotched samples and 345 MPa (50 ksi) for notched samples simulating real world scenarios. [21]

Element	Minimum %	Maximum %
Fe	Balance	
Ni	50	55
Cr	17	21
Nb	4.75	5.5
Mo	2.8	3.3
Ti	0.65	1.15
Al	0.2	0.8

Table 3.1: Powder Chemical Composition wt-% [54]

The specimen samples received were manufactured in-house at a University lab using Laser Powder Bed Fusion (LPBF) technique using an EOS M290 metal 3D printer, with virgin IN718 powder feedstock. Four cylindrical specimens, labelled B7, B10, C3, and C12,\* were selected from the batch as represented in figure(i), after which all samples underwent different combinations of Hot Isostatic Pressing (HIP) in argon filled furnace and heat treatment (HT) processes for adequate precipitate formation. Specimens were already tested for their fatigue life performance at uniaxial tension-compression loading stress of 700 MPa and the results obtained are stated.

#### Fatigue life results of the Inconel sample

B7 : 60233 cycles
 B10 : 68889 cycles
 C12 : 342709 cycles
 C3¹ :1242612 cycles

<sup>&</sup>lt;sup>1</sup> \*Nomenclature of the selected samples are based on the locations on the print bed

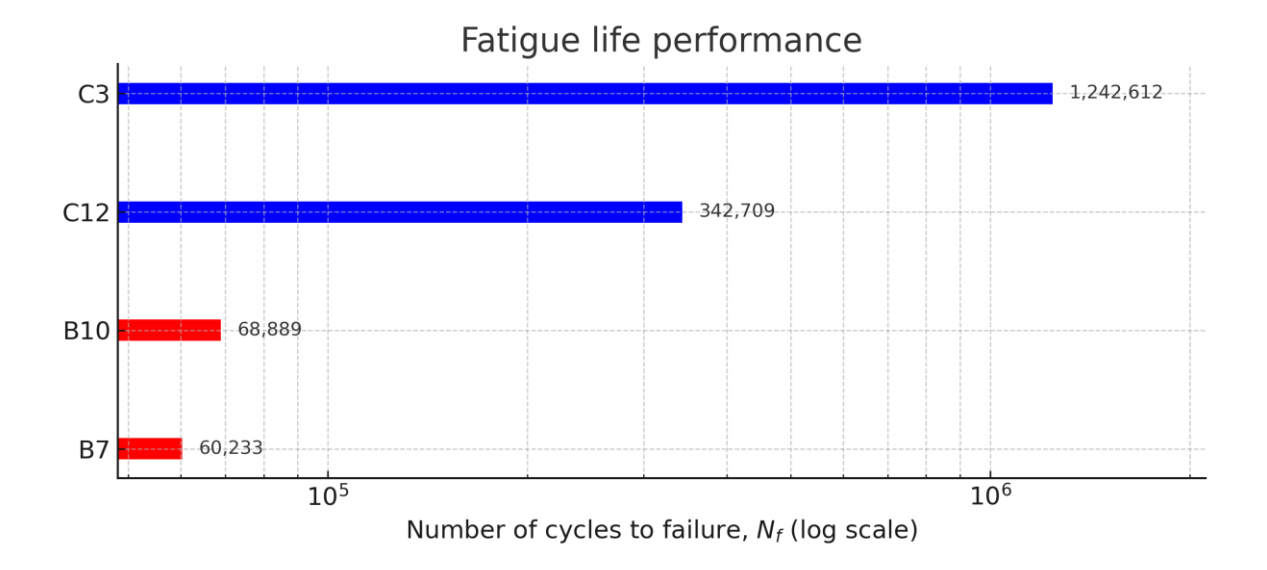


Figure 3.1 Fatigue life of all the four samples

#### 3.2 Methodology

The study employed a multi-technique approach for the microstructural characterization of the LPBF-fabricated IN718 samples. Summarised below is the methodology followed throughout the research work, **detailed explanation is followed in subsequent sections** about the entire work carried out for the research according to various ASTM standards and procedures.

#### - Sample Preparation

To ensure reliable and reproducible characterization, the specimens were carefully prepared following standard metallographic ASTM protocols. Each step of the preparation was selected for exposing a representative cross-section of the material with precaution and care. The preparation procedure ensured to achieve a smooth surface free of defects to reveal IN718 alloy's microstructure under various advanced microscopes.

- 1. **Sectioning**: Cross-sectional slices were taken from the mid-height of each cylindrical specimen to capture a uniform microstructural region.
- 2. **Mounting**: Samples were mounted using conductive epoxy resin to provide stability during further analysis.
- 3. Grinding and Polishing: Carried out as per ASTM E3-11:
  - Sequential grinding using SiC papers (320 to 1200 grit)
  - o Polishing using diamond suspensions (6 μm to 1 μm)
  - o Final polish using colloidal silica (0.04 μm)
- 4. **Etching**: Kalling's No. 2 etchant which is a solution mixture prepared of 5 g CuCl<sub>2</sub>, 100 ml HCl, 100 ml ethanol following ASTM E407 standard to reveal grain boundaries and secondary phases

#### - Characterisation Technique- SEM and EDS Analysis

- High-magnification SEM imaging was conducted to assess surface morphology, porosity, and to identify various phases present in the material.
- EDS spot and mapping analysis were performed to determine the composition of matrix, carbides, Laves phase, and δ-phase and to verify if it corresponds to the literature.

#### - Mechanical Testing

- Hardness tests were conducted using a Vickers indenter with 10 kgf (HV10) load, with a dwell time of 10 seconds.
- Ten indentations per sample were averaged later for statistical relevance.

#### - Image Analysis and Phase Quantification

- **ImageJ** was used to threshold and calculate total porosity (%) from polished SEM images.
- Weka Segmentation was trained on manually labelled areas (matrix, Laves,  $\delta$ -phase) and applied to 10 images per sample to quantify phase fractions.
- MATLAB scripts were used to calculate measurements for grain size cumulated and averaged from ten images of each the four samples via the linear intercept method.

#### 3.2.1 Metallography Sample Preparation

The four Powder Bed Fusion Laser Beam (PBF-LB) Inconel 718 specimens (C3, C12, B7, B10 \*²) were prepared for metallographic examination at the lab figure 3.2 with the dual objectives of preserving the microstructural features of the additively manufactured billets and enabling reproducible, quantitative measurements. Because PBF-LB IN718 exhibits layer-wise anisotropy usually along build-direction columnar grains and heterogeneous carbide/Laves/δ-phase distributions, the preparation route was designed to minimize thermal and mechanical disturbance while maintaining strict orientation control. Rigorous cleaning steps prevented abrasive carryover, and acceptance criteria for uniform scratch replacement. The resulting surfaces were suitable for optical microscopy, FEG-SEM imaging, EDS mapping, and supporting quantification of porosity, grain size, and NbC/secondary-phase distributions and enabling correlation with hardness and fatigue performance. Preparation principles figure 3.3, aligned with ASTM E3 and etching/characterization practices guided by ASTM E407.

\_

<sup>&</sup>lt;sup>2</sup> \* Nomenclature of the selected samples are based on the locations on the print bed



Figure 3.2 Metallography preparation lab

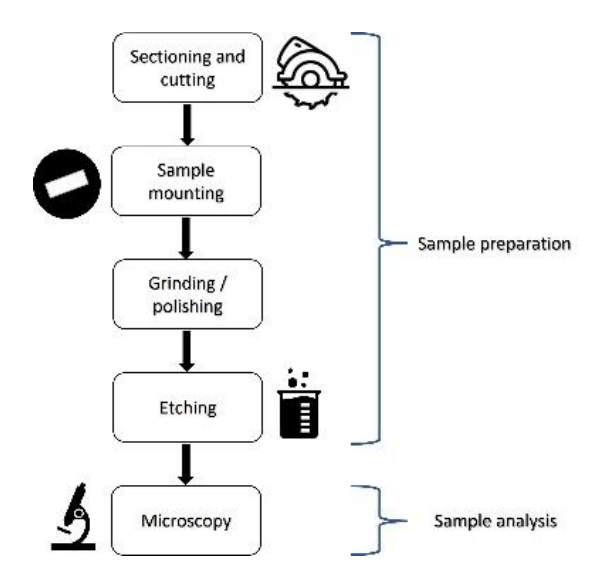


Figure 3.3 Sequence of metallography procedure

#### 3.2.1.1 Sectioning and Cutting





Figure 3.4 Cutting machine and samples cut in XY and XZ plane

All four Inconel 718 specimens (B7, B10, C3, C12) were sectioned on a Buehler precision abrasive cutter figure 3.4 using an aluminium-oxide cut-off wheel (40Al-15), operated at a spindle speed of 3000 rpm with an automatic feed rate of 4mm/min. Wet cutting was employed throughout, with a water-miscible cutting fluid mixed with deionized water at the manufacturer recommended concentration to ensure efficient heat removal, chip flushing, and corrosion inhibition during sectioning. The coolant was directed in a balanced flow on both sides of the wheel to maintain uniform temperature at the cut face and to reduce the risk of wheel glazing, uneven wear, or burr formation.

The choice of an Al<sub>2</sub>O<sub>3</sub> abrasive for sectioning Ni-based superalloys is consistent with established metallographic practice for ferrous systems in the 200-500 HV range, alumina wheels are widely recommended for steels and superalloys, whereas SiC wheels are preferentially used for non-ferrous alloys.

Specimens were rigidly fixtured in a low vibration jig with soft jaws and a backing to support the exit side of the cut and to avoid edge chipping. The contact area between the wheel and the workpiece was minimized by orienting each sample so that the wheel engaged a narrow section. Feed rate and downforce were kept conservative to avoid burning or work-hardening at the surface both of which can obscure true microstructural features.

A cutting plane figure 3.5 was defined to preserve orientation for further analyses. For each specimen, two orthogonal planes were prepared (i) a longitudinal plane parallel to the build direction (Z) to examine melt-pool columnar grains along BD, and (ii) a transverse (XY) plane to assess features across layers. Orientation marks were scribed on the gauge region

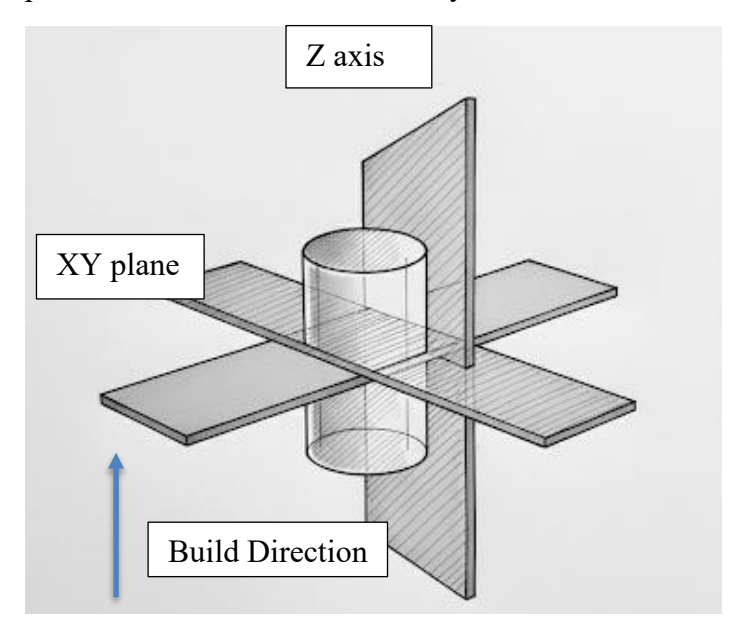


Figure 3.5: Cutting Section Plane

prior to sectioning, and all labels (sample ID and build direction arrow) were transferred to the cut faces. This approach facilitates reproducible comparison of porosity distribution, grain size, and carbide morphology between BD and transverse sections in later microscopy and image-analysis steps. General metallographic guidance emphasizes careful selection of sectioning planes and preservation of orientation.

Two pieces were prepared for mounting from the given billet material of diameter  $\varnothing$  10 mm, cut with 8 mm thickness in the build direction (BD $\odot$ ), while other having a thickness of 12 mm, which is cut again laterally into two facing XY direction (Perpendicular to Build Direction BD $\uparrow$ )

Section integrity and absence of cutting damage were verified immediately after sectioning. As recommended in metallographic standards the freshly cut surfaces were inspected under low-magnification optics to check for heat tint, smearing, microcracking, or pull-out; any evidence of thermal damage would necessitate parameter adjustment (lower feed, improved coolant delivery, or a softer bond wheel) and re-sectioning. Notably, abrasive wet cutting is recognized to introduce the least damage for the time invested when coolant flow is adequate. [55]

Cut parts were rinsed with deionized water, followed by an ethanol rinse and oil-free air drying to remove residual coolant and particulates. Edges were lightly dressed to remove burrs while avoiding any alteration of the region of interest. Subsequent steps (mounting, grinding, and polishing) were performed in accordance with ASTM E3 guidance to reveal the true microstructure without introducing preparation artifacts, an essential requirement for accurate quantification of porosity, grain size, and NbC precipitate area fraction, as well as for reliable hardness and fatigue correlations.

Overall, the selected wheel, conservative feed and speed, balanced coolant delivery, and orientation controlled fixturing constitute a sectioning protocol aligned with best-practice guidelines for metallographic preparation of ferrous alloys and superalloys, aimed at preserving the as-built or heat-treated microstructure for subsequent quantitative characterization.

#### 3.2.1.2 Sample Mounting preparation



Figure 3.6 Mounting Machine

Specimen mounting was done on a Struers hot-compression mounting press figure 3.6 using a type of resin known as PolyFast, which is a thermosetting phenolic Bakelite resin with carbon filler that provides low shrinkage, good edge retention, and electrical conductivity, having an advantage for subsequent SEM/EDS examination and for minimizing interfacial gaps that can bias quantitative image analysis. For each 30 mm mount, 15 mL of PolyFast powder was dispensed around the specimen using a spatula, and the instrument's system-defined PolyFast cycle was used: setpoint temperature 180 °C, axial pressure 250 bar applied via the press ram, and a heating dwell of approx. 3.5 min. Mounts were then cooled under pressure for around 1.5 min before ejection. These setpoints align with Struers selection guide for PolyFast at 30 mm diameter; the resin quantity is specimen-dependent Struers lists 20 mL as a nominal fill for a 30 mm mount with 20 vol% insert, and here was adjusted to achieve the target mount height while fully encapsulating the gauge section. [57]

Prior to charging the cylinder, specimens were cleaned to remove cutting coolant and debris to promote proper wetting and adhesion of the resin around edges an ASTM E3 recommendation to avoid contamination. The sample was centered in the 30 mm mold to ensure uniform wall thickness were transferred onto the mount edge to preserve specimen orientation for longitudinal and transverse (XY) analyses in later steps. A consistent axial

load and a high cooling rate under pressure were maintained to minimize polymerization shrinkage and prevent voids at the specimen–resin interface. Cooling under pressure is specifically advised for thermosetting mounts to avoid cracking and edge separation, thereby preserving true edge geometry for porosity, grain-size, and carbide metrics. [56]



Figure 3.7 Mounting preparation

The choice of PolyFast was due to its technical advantage. First, low-shrinkage, edgeretentive mounts preserve the as-prepared edge, reducing rounding during automated grinding and polishing and improving the fidelity of stereological measurements. Second, the carbon filler imparts bulk conductivity, which reduces charging in SEM and allows reliable high-magnification imaging and X-ray microanalysis without extensive surface metallizationespecially useful when multiple etch/inspect cycles are planned. Struers explicitly recommends PolyFast for SEM work on hard and medium-hard metallic materials for these reasons. [57]

Process control followed vendor guidance for hot mounting. The press was loaded with the lower ram lubricated or treated with an approved anti-stick where necessary resin powder was poured to form a base, the specimen was positioned with the region of interest facing the intended preparation surface, and the remaining powder was added to fill the mould. The automated cycle then executed heating, dwell, and pressured cooling. The resulting mounts exhibited the expected hardness and dimensional stability for subsequent grinding/polishing, consistent with Struers' hot-mounting process window for PolyFast.

Health, safety, and environmental precautions were observed per the PolyFast Safety Data Sheet: dry handling of powder to limit dust, local extraction with adequate suction ventilation, gloves and eye protection during loading/unloading, and care to avoid inhalation of dust and fumes; hot mounts were allowed to cool under pressure and were ejected using heat-resistant gloves. Resin was stored in a cool, dry place in the original container per SDS guidance. [57]

Overall, hot compression mounting at 180 °C/250 bar/3.5 min (with pressured cooling) using PolyFast produces dimensionally stable figure 3.7, conductive 30 mm mounts with excellent edge retention, consistent with ASTM E3 guidance and Struers' documented parameters, and provides a robust support base for accurate microstructural characterization and mechanical property correlation.

#### 3.2.1.3 Grinding & Polishing

Grinding and polishing were performed using a standardized Struers MD/DiaPro figure 3.8 prepared for hard Ni-based alloys. Plane and fine grinding were used to remove sectioning damage and establish a flat, deformation-limited surface prior to polishing which mirror finishes the surface for critical microscopic analysis. This sequence produces planeness while minimizing relief on multiphase Ni-based alloys. After each step, the surface was inspected to confirm uniform scratch orientation across the mount figure 3.9, absence of residual cut marks, and no edge rounding only then was the next, finer abrasive used. The approach and acceptance criteria follow established metallographic guidance for grinding/polishing workflows and for preparing hard superalloys for quantitative microscopy.[58]



Figure 3.8 Grinding machine

#### Plane Grinding PG

Plane grinding was performed on a rigid platen with an appropriate coarse abrasive capable of eliminating cut marks within a few minutes, followed by fine grinding on a hard, metal-backed cloth with 9  $\mu$ m diamond suspension under controlled load and unidirectional rotation of the disc wheel. Two steps of Silicon Carbide SiC Emery Paper #220 (65  $\mu$ m) for wet grinding of materials (HV30-800) Plain Back and #500 (30  $\mu$ m) SiC paper on a surface of MD-Piano prepared in single sample guide setup in the machine with RPM Disc/Holder; 150/150, unilateral wheel rotation, a force of 30N each, water as lubrication, time of about

5 min initially and until obtained a plane surface. Grinding the edges before plain grinding for smooth operation done as recommended.[58]



Figure 3.9 Samples after polished and cleaned

Fine grinding and Polishing were performed using a standardized Struers MD/DiaPro route tailored to hard Ni-based alloys. Fine grinding used an MD-Allegro surface with DiaPro Allegro 9 µm suspension for 5 min at Disc/Holder 150/150 rpm in a unilateral (unidirectional) mode, applying 30 N per specimen. This rigid cloth/suspension pairing promotes rapid planarization with low subsurface deformation, ensuring flatness ahead of polishing. Polishing step 1 (DP1) employed MD-Dac cloth with DiaPro Dac 3 µm suspension at the same kinematics (150/150 rpm, unilateral) and 30 N for 5 min to remove 3 μm scratches while preserving planarity. **Polishing step 2 (DP2)** used MD-Nap cloth with DiaPro Nap B, 1 µm suspension for 2 min at 150/150 rpm, unilateral, 30 N, to eliminate residual micro-scratches. Between every step, specimens and mounts were rinsed and ethanol-washed using ultrasonic baths and if necesary with lint-free swabs to prevent abrasive carryover. Scratch orientation and uniformity were verified before advancing, consistent with metallographic best practice. A final chemical mechanical polish with 0.05 μm colloidal silica (OPS) removed the last deformation and enhanced phase delineation, yielding a surface suitable for quantitative image analysis and EDS. The cloth-suspension compatibilities and process logic follow Struers recommendations, while the cleaning/verification protocol aligns with ASTM E3 guidance.[56][58]

#### 3.2.2 Etching Technique



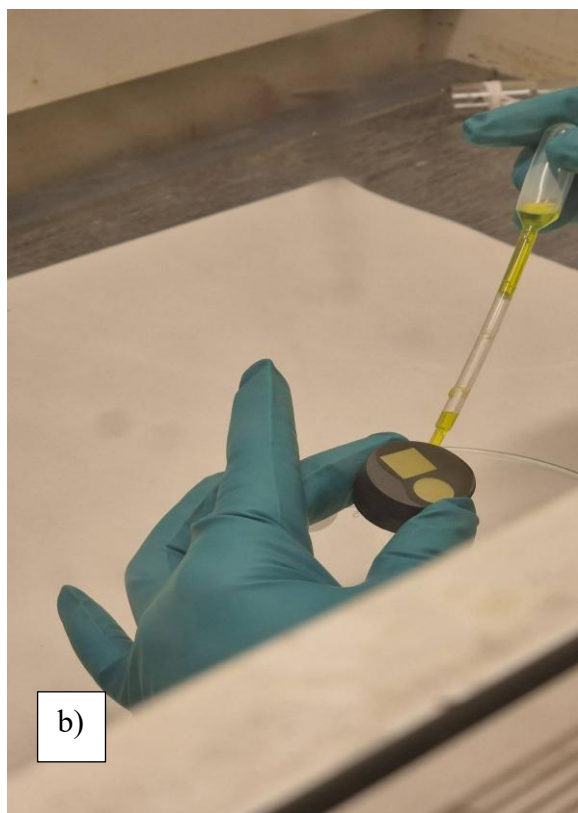


Figure 3.10 (a) Etchant preparation and (b) sample being etched.

Kallings waterless 2 reagent is prepared by mixing 100 ml HCl and 100 ml Ethanol (99%) then adding 5 gm CuCl<sub>2</sub> slowly with homogenous stirring, figure 3.10(a). This is an etchant commonly used to reveal microstructure in Nickel based superalloy. Etching was done for approximately 20–30 seconds in few drops with the help of a pipette, care was particularly taken to avoid over-etching of the sample by careful observation of colour changes, figure 3.10(b). Kallings 2 is effective in microstructural revelation of grain boundaries and exposing dendritic segregation, as well as enhancing contrast between phases like  $\delta$  and Laves under SEM imaging.

## 3.3 Microstructure Characterisation

#### 3.3.1 Microscopy

An optical microscope (Zeiss) figure 3.11(a) equipped with 5×, 20×, and 50× objective lenses was used for initial microstructural examination and quantitative image analysis. The microscope was fitted with a motorized stage connected to a computer interface, enabling precise positional control and automated image stitching to generate high-resolution, full-field micrographs of the specimens, figure 3.11(b).

For each sample, approximately 20 micrographs were captured at predetermined locations to ensure adequate sampling of the microstructure. This large dataset was necessary to achieve greater statistical accuracy in quantitative evaluations, such as grain size measurements, and porosity analysis.

The stitched panoramic images allowed for the assessment of microstructural uniformity across larger areas than could be observed in a small field of view, which thereby helped in comparing microstructural features among the samples with differing post treatments while also preserving high magnification detail for localized analysis. These images were later processed using dedicated image analysis software like Image J to extract relevant metrics.



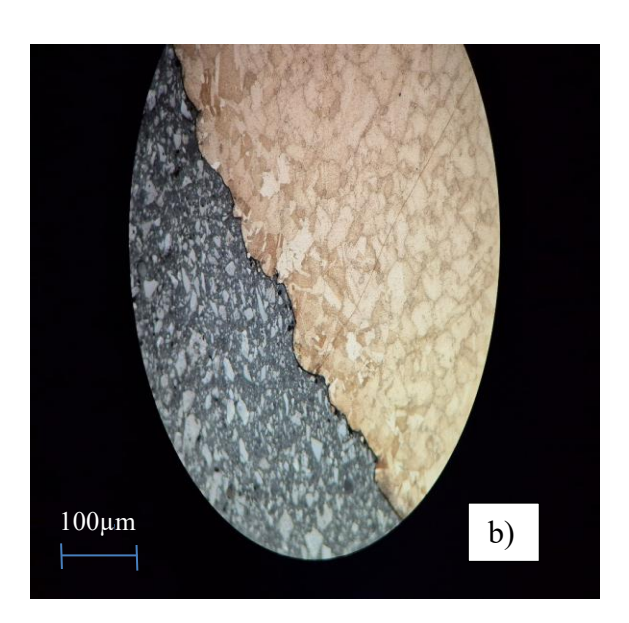


Figure 3.11 (a) Picture of an optical microscope device (b) Image captured using the microscope.

# 3.3.2 Field Emission Gun - Scanning Electron Microscopy (FEG-SEM)

A Gemini I550 FEG-SEM machine is employed to obtain more detailed and fine resolution images magnified up to 15000X, with an aperture size set to 60  $\mu$ m for EDS analysis later, electron beam accelerating voltage of 20 kV and 5 kV for reducing interaction volume of the surrounding particles for imaging micro and nanoscale precipitates such as  $\gamma$ ',  $\delta$  phase, Laves phases, other inclusions like Oxides(TiO) and Carbides (NbC) using Backscattered Electron detectors and secondary electrons. The chemical composition is verified using Energy Dispersive Xray Spectroscopy (EDS) using point analysis and area mapping to analyse the elemental composition of particles.

Microstructural characterization for further classification and critical analysis was performed using a Gemini class 1550 Field Emission Gun Scanning Electron Microscope (FEG-SEM) to obtain high-resolution images and detailed phase morphology. Imaging was conducted at magnifications up to 15,000X, allowing observation of fine microstructural features and nanoscale precipitates.

The machine had the specifications of varying accelerating voltage from 100V to 30kV, Low Vacuum operation (5-100 Pa) having detectors such as In-lens secondary electron (SED), Everhart-Thornley secondary electron (SED), Robinson-type back-scatter electron (BSED). Secondary & backscattered electrons and X-rays, light (for Cathodoluminescence) and Electron Beam Induced current (EBIC). Energy Dispersive X-ray Spectroscopy (EDS), Oxford INCA Energy E2H with INCAx-act 51-1385-005 Silicon Drift detector (SDD), Energy Resolution Mn K – 133eV, detection B - U, 0.1 - 1 at%. HKL Nordlys II Electron Back Scatter Diffraction (EBSD) system, including a Forward Scatter Electron (FSE) detector for additional studies.

An aperture size of  $60 \mu m$  was selected to provide optimal beam current for subsequent Energy Dispersive X-ray Spectroscopy (EDS) analysis. The accelerating voltage was adjusted based on the analysis requirements:

- 20 kV for EDS acquisition to ensure sufficient X-ray generation for elemental analysis.
- 5 kV for high-resolution imaging to minimize the electron interaction volume, thereby enhancing surface sensitivity and enabling clearer visualization of nanoscale precipitates.

Imaging was carried out using both Backscattered Electron (BSE) and Secondary Electron (SE) detectors:

- BSE mode was used for phase contrast imaging to distinguish between  $\gamma$ ',  $\delta$  phase, laves phase, and other inclusions such as oxides (TiO) and carbides (NbC) based on atomic number differences.
- SE mode was used to examine fine surface morphology and topographical details of the matrix and precipitates.

Pictured below figure 3.12 is the actual SEM images used for the EDS point analysis, which is very crucial for understanding the chemistry and the elemental composition within the microstructure to verify with the literatures and to further use for the quantification study.

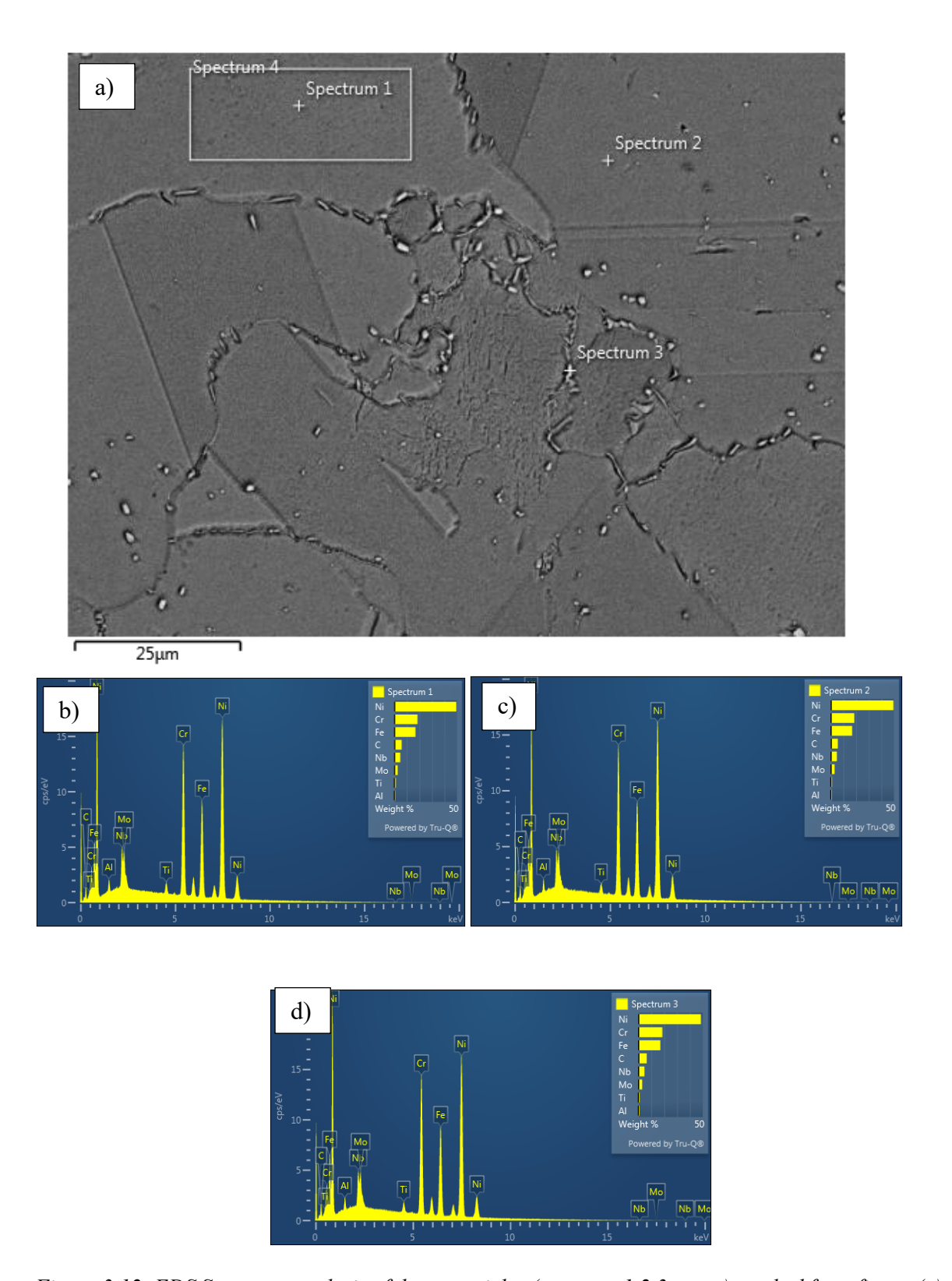


Figure 3.12: EDS Spectrum analysis of three particles (spectrum1,2,3, resp.) marked from figure (a).

**Energy Dispersive X-ray Spectroscopy** (EDS) was employed for chemical composition verification of observed features. Both point analysis and area mapping were conducted, figure 3.13(b)

- Point analysis was used to determine the elemental composition of individual precipitates or inclusions.
- Area mapping provided a spatial distribution of elements, enabling correlation between specific phases and their compositional profiles.

This combined FEG-SEM and EDS approach facilitated the identification and characterization of microstructural constituents, supporting the correlation between microstructural features and the mechanical behaviour of the Inconel 718 samples.

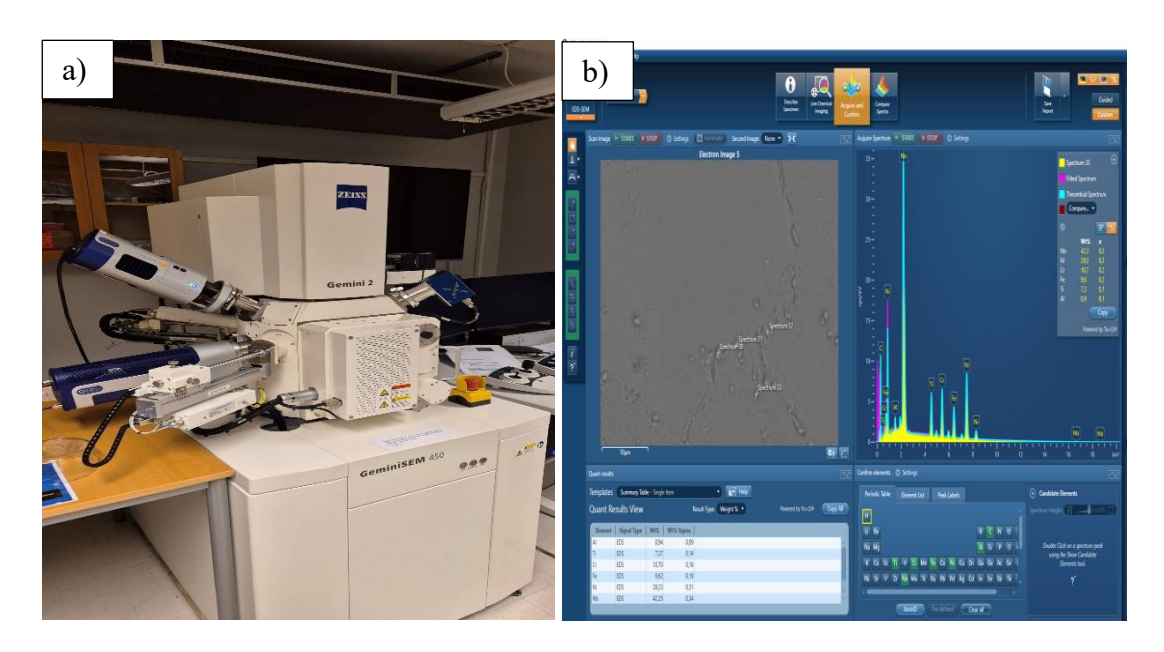


Figure 3.13 (a) Picture of a SEM machine and (b) EDX software window.

#### 3.4 Vickers Hardness Testing

Vickers Hardness testing followed ASTM E384 hardness method. Prior to testing, all metallographic specimens were prepared through standard grinding and polishing procedures as explained in the above sub section to ensure a smooth, deformation-free surface suitable for indentation. A 10 kg force of load was applied with a dwell time of 10 seconds for each measurement to minimize elastic recovery effects and obtain consistent impressions.

Distance from the edge of the sample is made sure of at least is 2.5 times the diagonal length from the specimen edge or any distinct observable microstructural feature boundary such as grain boundary clusters, pores, etc. figure 3.14. This procedure as recommended by the ASTM E384 standards ensures that the plastic deformation field beneath one indent does not influence the hardness reading of another or can cause *strain hardening* or altered stress distribution, which may cause error in measurement readings. This was pre-fed into the system used by hardness test machine and a continuous testing with less human errors were obtainable for an error-free result.

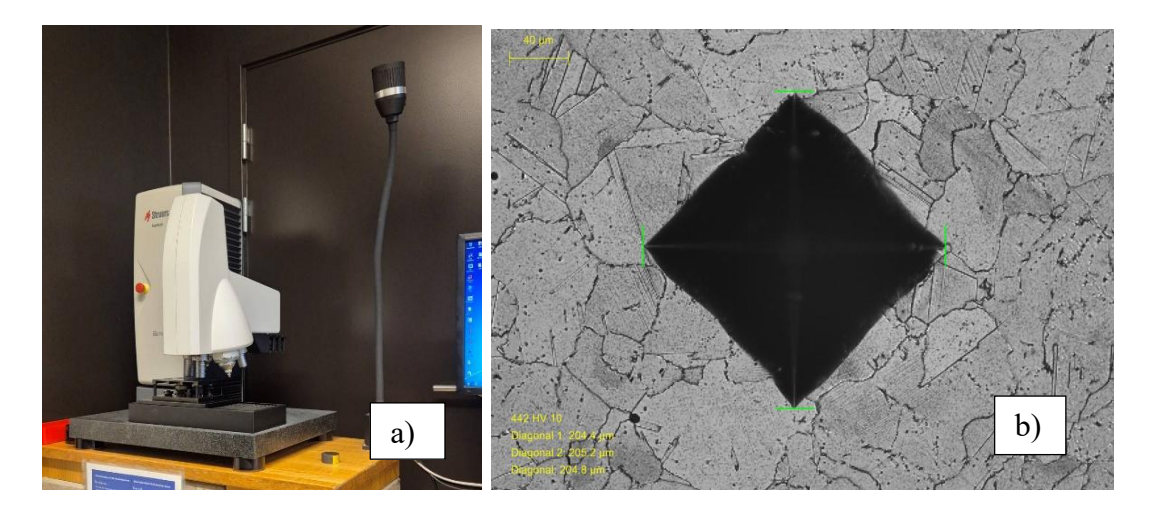


Figure 3.14 (a) Hardness Testing Device, (b) Microscopic Image of the indentation.

#### 3.5 Fatigue Testing

Uniaxial push-pull fatigue tests performed at room temperature under controlled amplitudes of stress at 700 MPa, in accordance with ASTM E606/E606M testing standards, specimens prepared as shown in figure 3.15. Two post process were done on the samples to find an optimum condition having better properties.

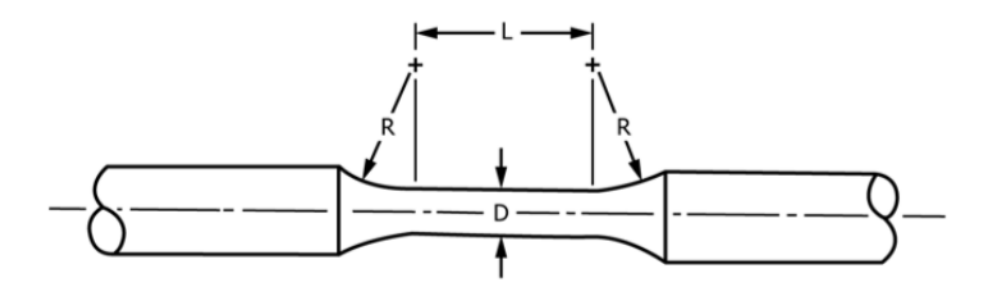


Figure 3.15 Specimens with fillets for fatigue tests.

1.Heat treatment- The Inconel 718 samples were subjected to a multi-step heat treatment to homogenize the microstructure, dissolve detrimental phases, and to precipitate strengthening phases. **Homogenization**: Samples were heated to 1200 °C held for 4 hours to reduce elemental segregation and dissolve Laves and  $\delta$  phases. **Solution annealing**: The furnace was then cooled to 1000 °C and held for 2 hours to achieve a supersaturated  $\gamma$  matrix and promote recrystallization. **Ageing**: Subsequently, the temperature was reduced to 700°C and held for 1 hour to precipitate  $\gamma'$  and  $\gamma''$  phases for hardening.

2. Hot Iso-static Pressing at 1100 -1200 °C at 100 MPa with argon filled chamber to prevent oxidation, which is a usual procedure for closing pores in the material. The test results obtained are summarised in table 3.2.

Sample	Post Process Fatigue life (no. of cycles to failu	
C3	HT+HIP	1,242,612
C12	HT	342,709
B10	HT+HIP	68,889
В7	HT	60,233

## 4 Results and Discussion

#### 4.1 Quantitative Analysis & Characterisation

#### Metal Carbide, MC-type precipitates

Quantitative image analysis of microstructural images from SEM figure 4.1, revealed possibly MC-type precipitates mainly Niobium Carbides (NbC) which was further verified with EDS point analysis across samples all of which are post processed (C3, C12, B7, B10) yielded volume fractions of 0.68%, 0.28%, 0.94%, and 0.35%, respectively, table 4.1. Sample C3 (HT+HIP) which achieved more than  $1.2 \times 10^6$  cycles is used as the internal reference to compare relative enrichment or depletion of NbC under post-processing conditions. After normalisation C12 have 41%, B7 with 138%, and B10 with 52% against C3 at 100%, table 4.1. This framing allows direct interpretation of how carbide content covaries with grain size, hardness, porosity, and fatigue life. Prior work on IN718 underscores that NbC is a persistent, thermally stable phase whose presence reflects solidification partitioning and subsequent heat-treatment history. Its fraction and size distribution influence grain-boundary stability and the allocation of Nb between carbides and the agehardening  $\gamma''$  phase (Ni<sub>3</sub>Nb). [43]

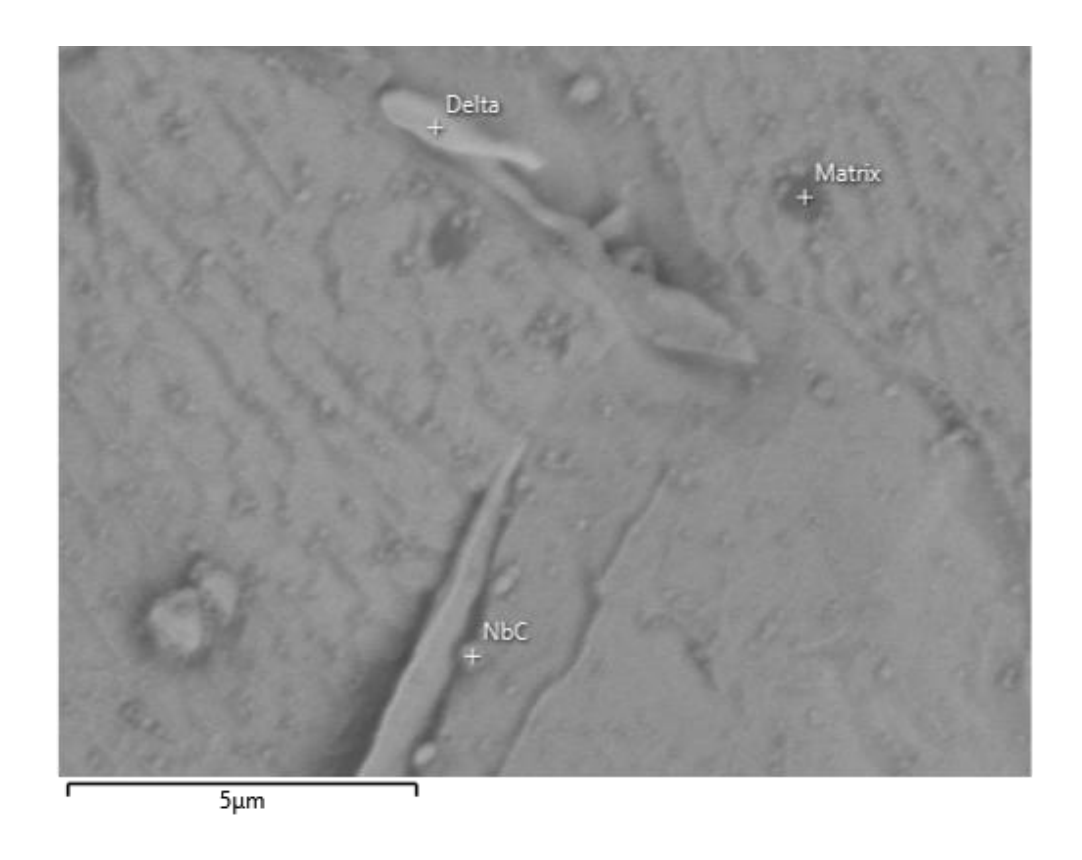


Figure 4.1 EDX mapping of specimen sample C3 post processed.

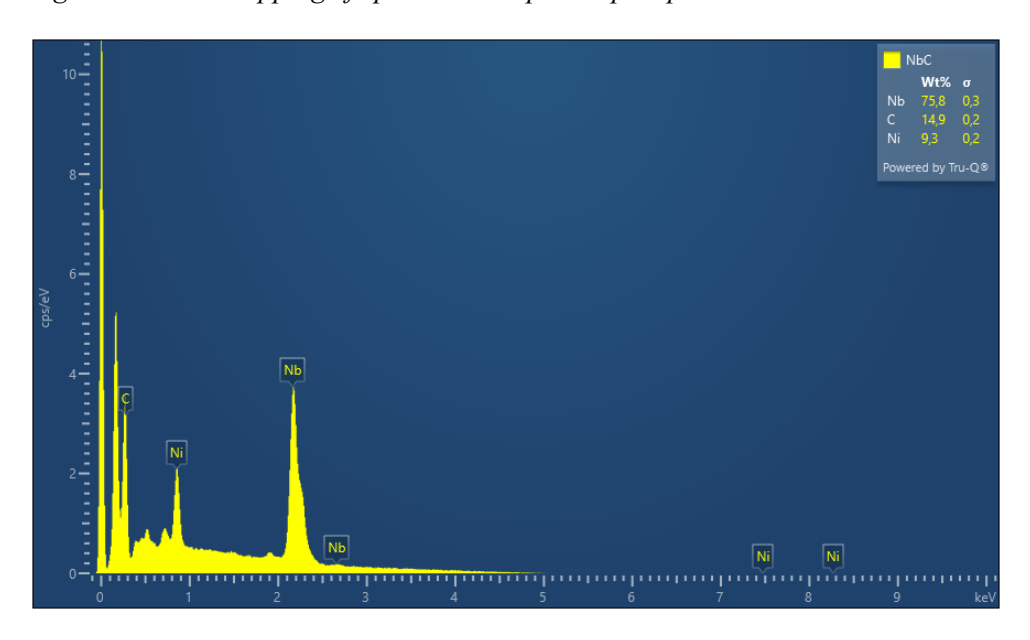


Figure 4.2: EDS analysis confirming NbC particle.

Sample B7 being analysed using SEM and EDS, figure 4.4 confirms the presence of metal carbide particles within the microstructure of the matrix.

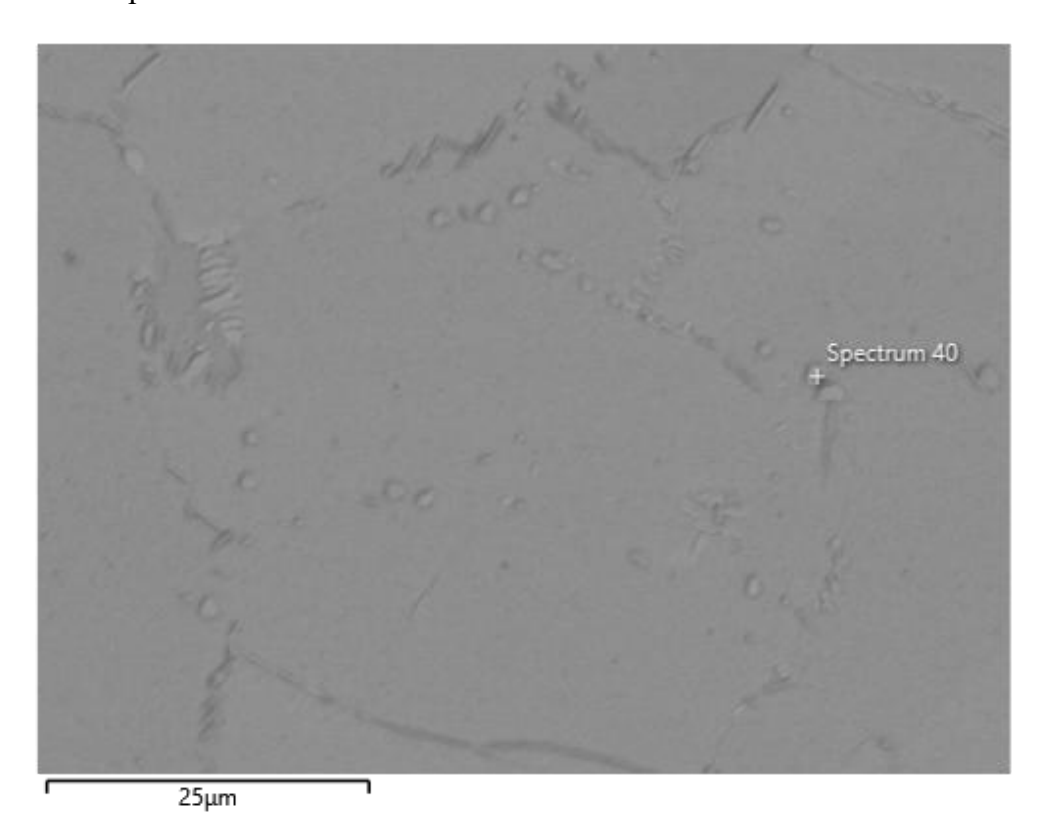


Figure 4.3 Specimen B7 at EDX analysis.

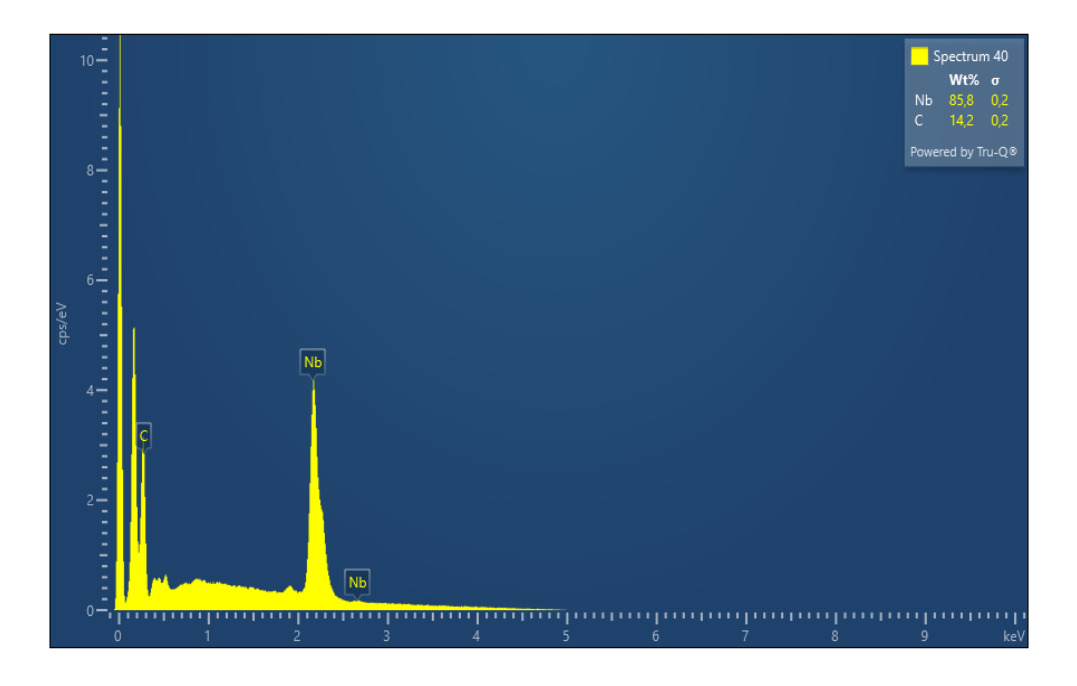


Figure 4.4: NbC is identified from the spectrum for B7.

Table 4.1: Measured NbC precipitate volume fractions and relative values to sample C3.

Sample	Volume %	Relative to C3 (%)
C3	0.68	100
C12	0.28	41
B7	0.94	138
B10	0.35	52

A higher content of NbC can increase grain-boundary pinning and thus reduce grain growth during thermal exposure. However, excess Nb from the matrix precipitated as NbC may deplete the Nb reservoir for  $\gamma''$ , moderating age-hardening strength. Both effects are well documented by Radavich and Zhao et al., for wrought and AM IN718, and particularly relevant after homogenization/HIP with aging heat treatment where Laves dissolution releases Nb back into solution for subsequent  $\gamma''$  precipitation. [42]

Sample C3's intermediate NbC volume (0.68%) represents a balanced state table 4.1, providing sufficient precipitates for grain stabilization without excessive Nb consumption, which is optimal for tensile strength and fatigue resistance, Zhang et al. Thus, C12 and B10 can be classified as "NbC-deficient," while B7 is "NbC-rich." These disparities likely stem from variations in solidification rates, segregation during powder bed fusion, or heat treatment (Chamanfar et al.).

#### Grain size and anisotropy

Grain size was measured along two orthogonal directions the build direction (Z) and the transverse plane (XY). The average values ( $\mu$ m) are presented in Table 4.2, along with normalized averages relative to C3 and anisotropy ratio (ratio between the two axes).

Table 4.2: Measured grain sizes.

Specimen	Build Direction (XZ) (µm)	Transverse Plane (XY) (µm)	Average Normalized to C3	Anisotropic Ratio a
В7	66	70	0.7	0.94
B10	113	116	1.2	0.97
C3	105	79	1.0	1.32
C12	83	86	0.9	0.96

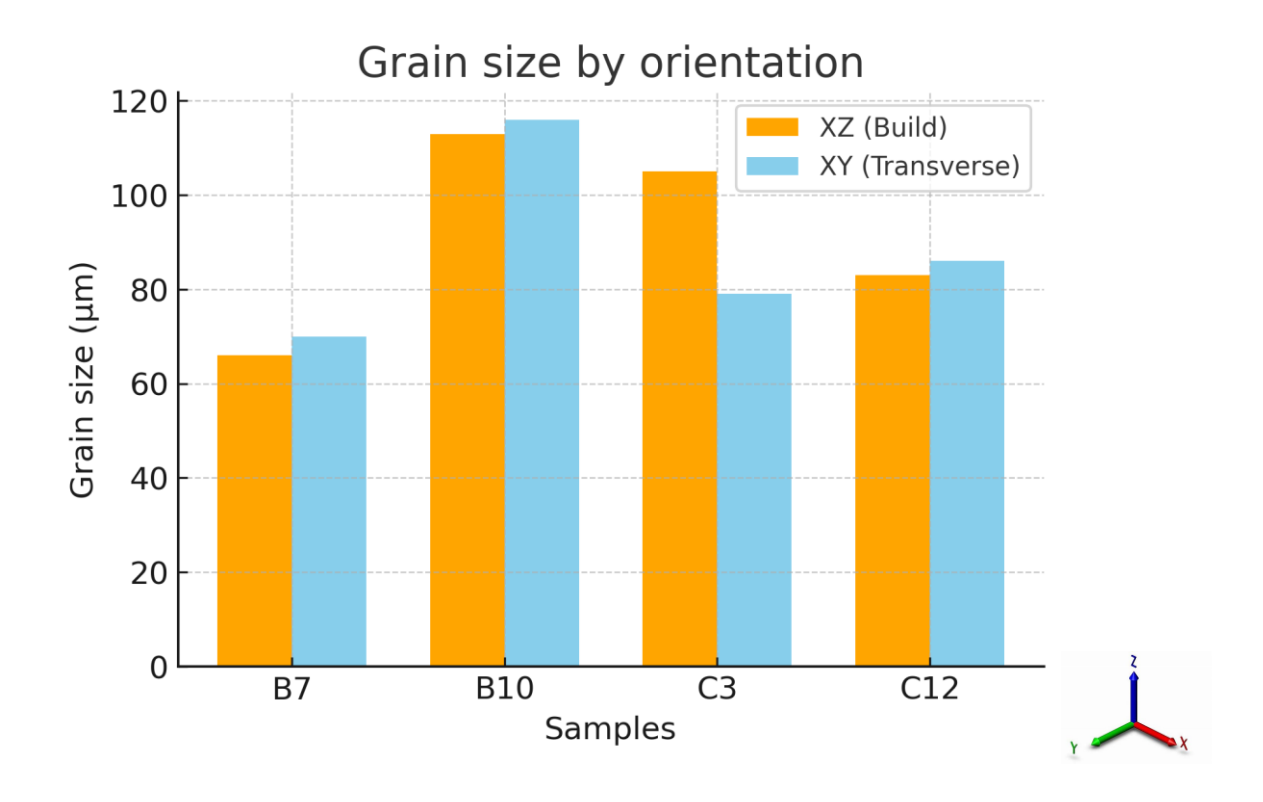


Figure 4.5: Grain size across orientation plane (XZ and XY).

Pictures below gives a comprehensive understanding of the differences in microstructure and various phases present across all the four samples B7(fig 4.6) which is only heat treated, B10(fig 4.7) which is HIPed, C3(fig 4.8) which is both heat treated and HIP and C12(fig 4.9) which underwent HIP, presented below to give valuable insight to compare.

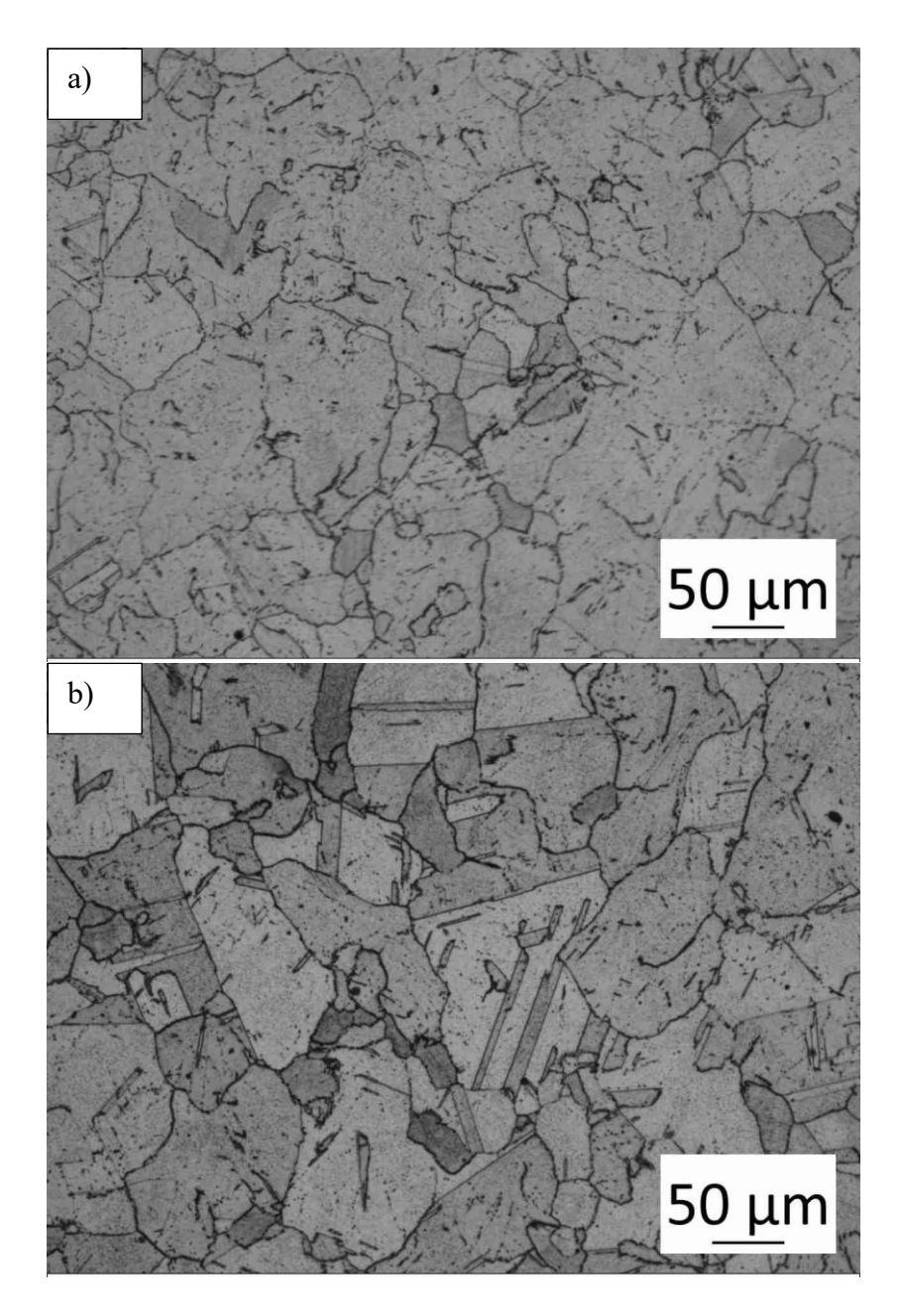


Figure 4.6: B7 (HeatTreated) micrograph along a) XZ and b) XY plane.

Micrograph of sample B10, Heat treated and HIP after etching using optical microscope for image analysis to reveal the microstructure and defect present in the material.

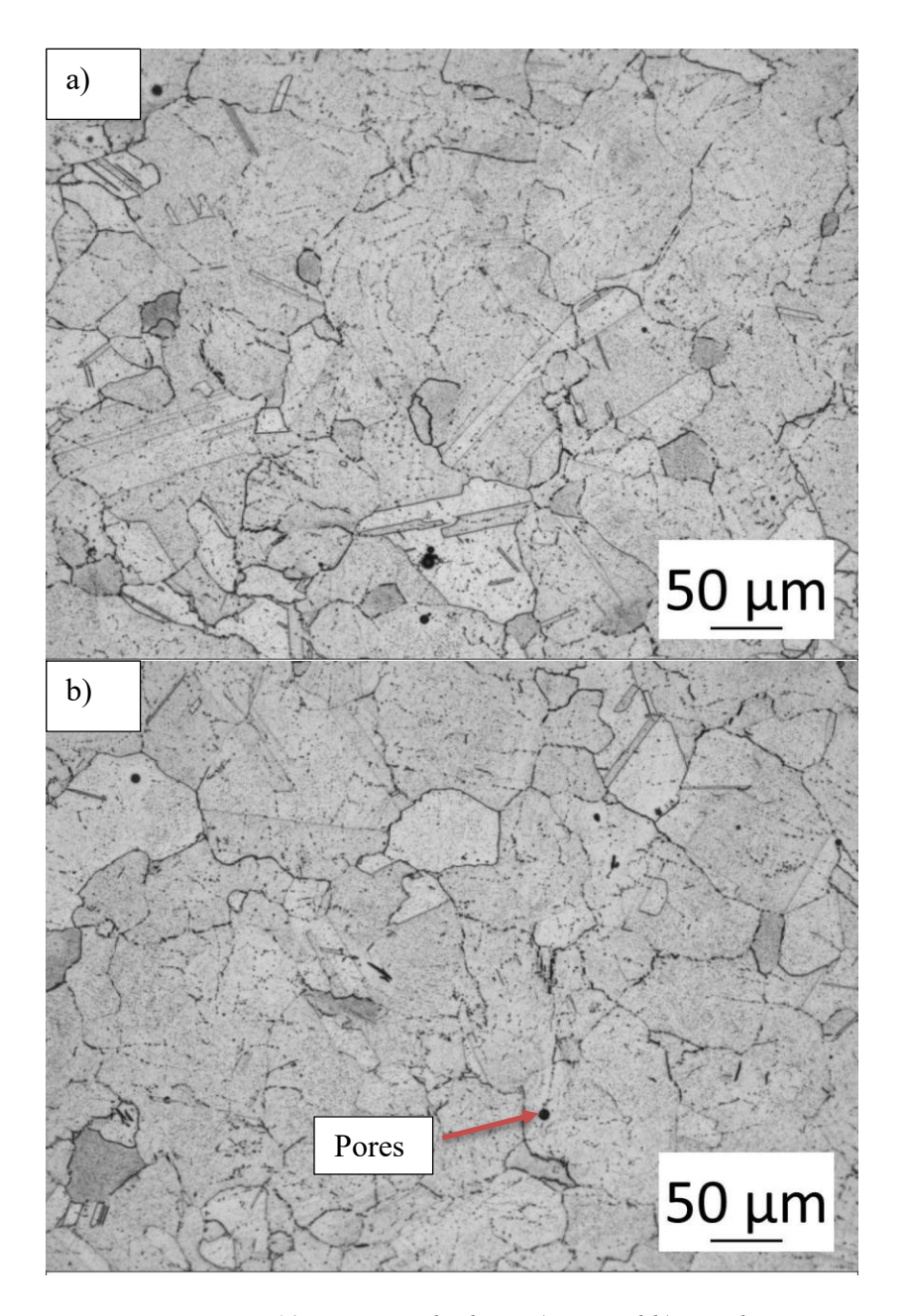


Figure 4.7: B10 micrograph along a) XZ and b) XY plane.

Micrograph of sample C3, Heat treated and HIP after etching using optical microscope for image analysis to reveal the microstructure and defect present in the material.

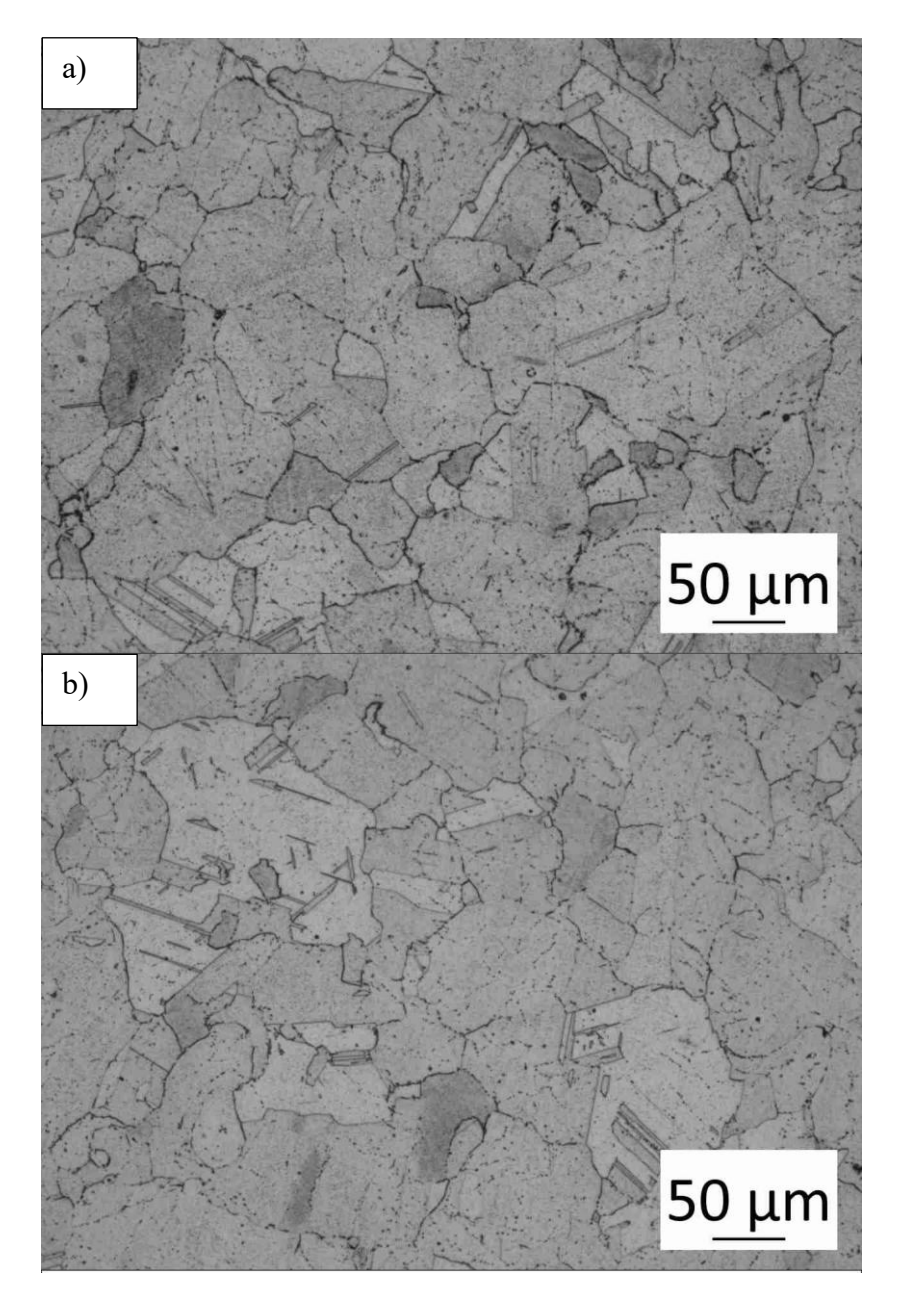


Figure 4.8: C3 micrograph along a) XZ and b) XY plane.

Micrograph of sample C12, Heat treated after etching using optical microscope for image analysis to reveal the microstructure and defect present in the material.

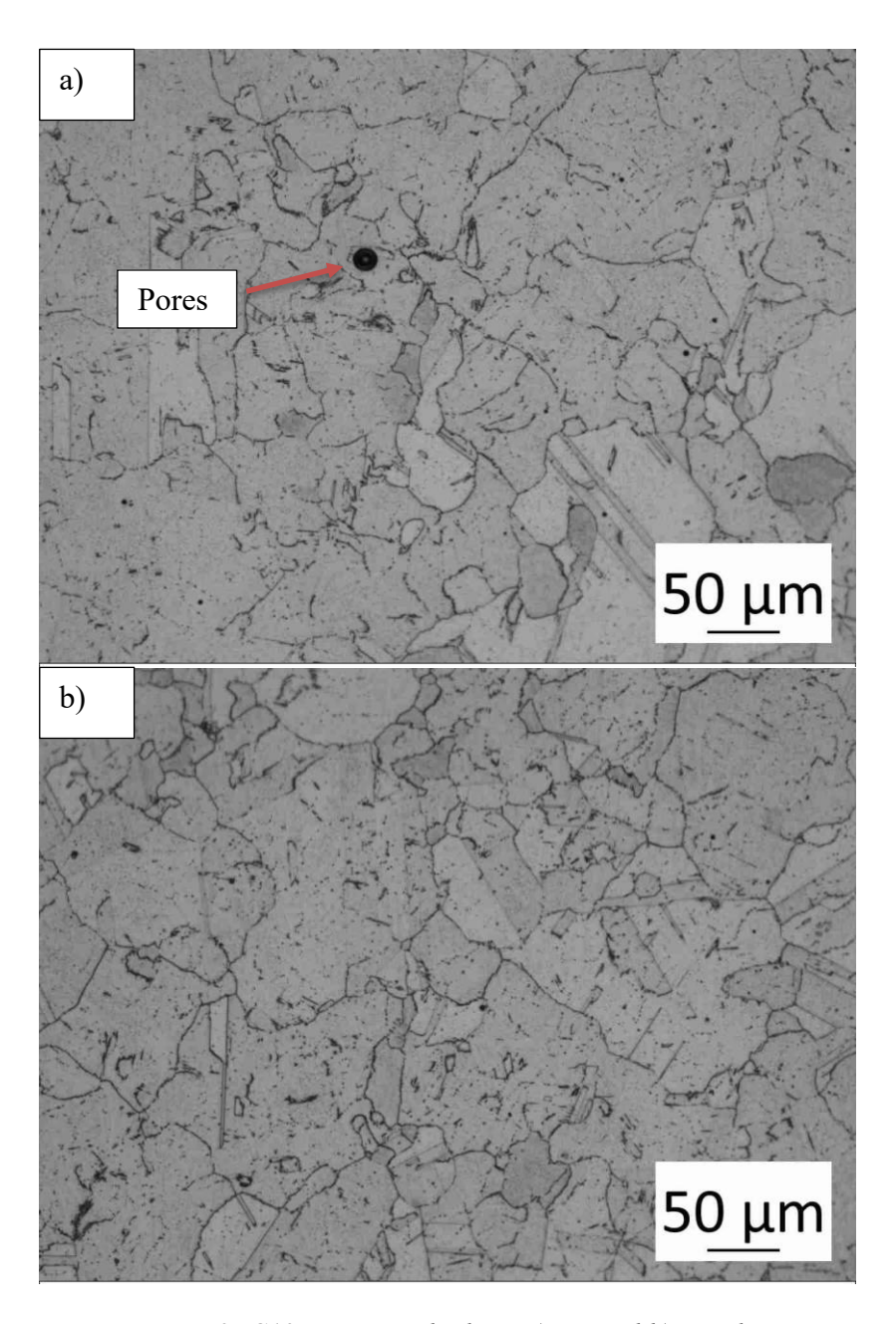


Figure 4.9: C12 micrograph along a) XZ and b) XY plane.

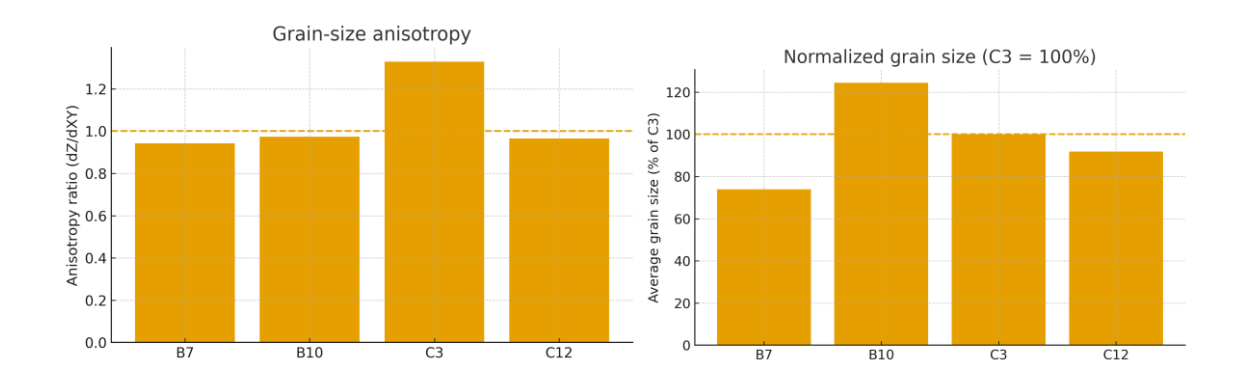


Figure 4.10: Grain-size anisotropy ratio, dashed line denotes isotropy.

It can be inferred that, B7 exhibits the finest, near-isotropic grains along both orientation, 66  $\mu$ m in Z, 70  $\mu$ m in XY. B10 exhibits the coarsest grains. C3 figure 4.8 exhibited notable anisotropy with Z-direction coarsening but comparatively finer XY grains, and C12 was intermediate with good isotropy (83  $\mu$ m in XZ, 86  $\mu$ m in XY). When {a >1} grains are elongated along Z axis, when {a <1} finer grains along Z axis, and {a  $\approx$ 1} for isotropic grains. This could be understood as variation from process parameters.

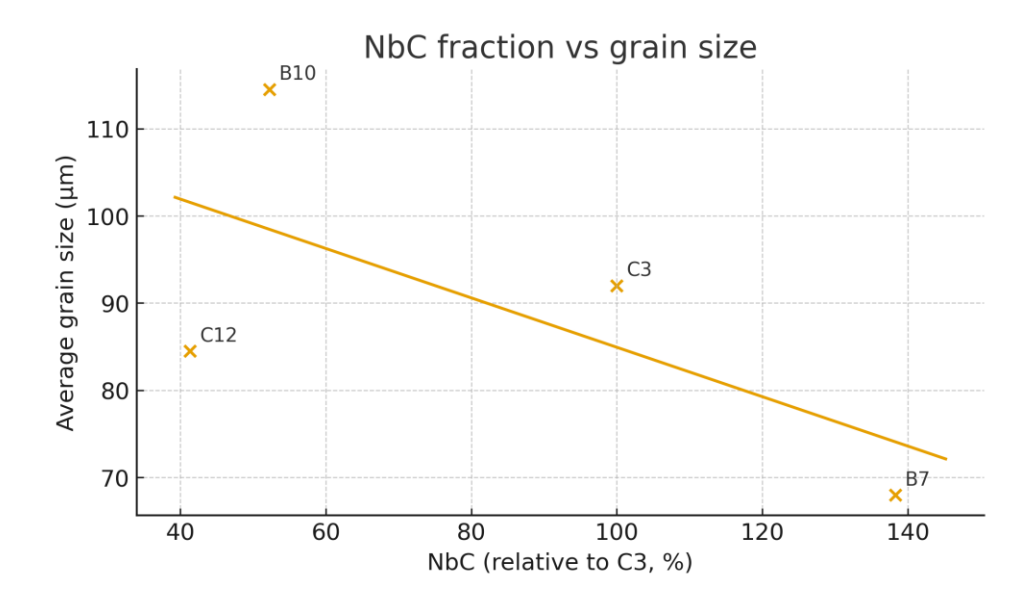


Figure 4.11: NbC (relative to C3) vs average grain size (linear trendline shown).

These variations reflect directional effects common in additively manufactured materials, such as thermal gradients and solidification rates B7's fine, isotropic structure suggests faster cooling, smaller melt pools, or enhanced grain boundary pinning by precipitates like NbC. B10's coarseness implies slower cooling or reduced pinning (NASA Technical Reports Server, NTRS).

#### **Role of Grain Boundary Pinning**

Grain size variations are primarily attributed to Zener pinning by NbC precipitates, a key mechanism in LPBF produced alloys. The Zener model predicts pinned grain size (D) as D = 4r / 3f, where r is particle radius and f are volume fraction, indicating an inverse relationship with precipitate fraction. B7's finer grains (66  $\mu$ m in Z, 70  $\mu$ m in XY) correlate with its high NbC (138% of C3), while B10's coarser grains (113-116  $\mu$ m) align with low NbC (52% of C3).

Anisotropy in C3 (ratio 1.32) suggests orientation-dependent pinning, possibly from NbC segregation in XY-plane melt pools, enhancing nucleation and restricting growth (Gallmeyer et al., Zhao et al.). Low porosity (0.006 -0.085%) supports effective pinning, as voids disrupt boundary-particle interactions. Near-isotropic hardness (440 HV10) indicates uniform NbC dispersion, with finer grains contributing to strength via Hall-Petch and Orowan mechanisms.[32]

Nb partitioning between  $\gamma''$  (Ni<sub>3</sub>Nb) and NbC influences this: higher carbon promotes NbC formation, pinning grains but depleting Nb for  $\gamma''$  (NASA Technical Reports Server). Precipitation kinetics in LPBF Inconel 718 further shape grain growth during aging or homogenization. The correlation between high NbC and fine grains in B7, versus low NbC and coarse grains in B10, supports pinning-controlled growth.

Per the Hall-Petch relation, finer grains enhance yield strength and hardness. B7's smallest grains predict higher yield than B10's coarsest, though texture modifies this in LPBF alloys. However, precipitate partitioning and porosity can offset grain-size effects (NASA Technical Reports Server). Normalized comparisons highlight practical significance: B7's 26% smaller grains (73.9% of C3) could have improved yield or fatigue, while B10's 24% coarsening (124.5% of C3) may degrade them. Porosity, even low, affects fatigue and hardness locally.

#### Hardness Relation with Microstructural Features

Vickers hardness was narrowly distributed (436-445 HV10) across orientations: A purely Hall–Petch model (finer the grain  $\rightarrow$  higher the strength) would predict B7 > C12 > C3 > B10 however, C3 exhibits the highest hardness than B7, indicating that various other factors such as precipitation phases ( $\gamma'/\gamma''$ ), local porosity near indents, and texture contribute alongside grain size. This behaviour is consistent with IN718 literature; hardness/yield are co-determined by  $\gamma''$  volume fraction and distribution, micro-segregation relief after HIP/solutionising, and residual porosity. It is possible to infer from our study that a high value of NbC is inessential to hardness/strength while a balanced amount as in case of C3 is beneficial.

Table 4.3: Summary of microstructural and Hardness metrics.

Sample	NbC (vol. %)	Grain Size (XZ) (µm)	Grain Size (XY) (µm)	` /	HV10 (XY) (mean ± SD)	Porosity XZ (%)	Porosity XY (%)
C3	0.68	105	79	$444.6 \pm 4.86$	$444.3 \pm 3.60$	0.006	0.013
B7	0.94	66	70	$436.3 \pm 2.33$	$437.3 \pm 5.36$	0.062	0.085
B10	0.36	113	116	$439.4 \pm 3.52$	$442.4 \pm 6.42$	0.013	0.016
C12	0.28	83	86	$439.6 \pm 2.45$	$439.6 \pm 4.07$	0.026	0.022

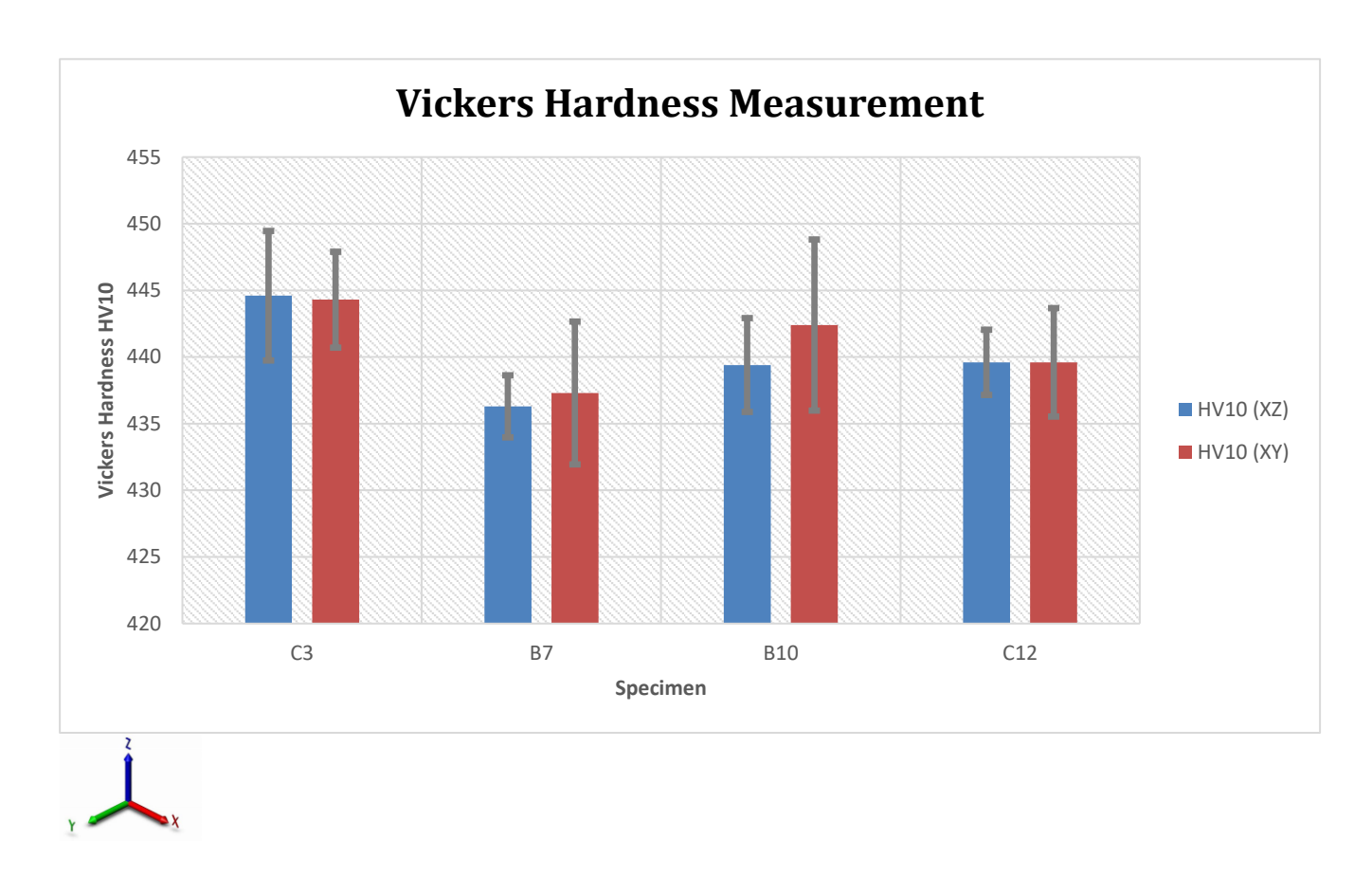


Figure 4.12: Vickers Hardness across four samples

A sequence could be made of post process treatment: (i) HIP/ageing dissolves Laves and homogenizes Nb; (ii) subsequent aging enables robust  $\gamma''$  precipitation; (iii) net hardness rises even if grain size is not the absolute minimum. This aligns with reports that Laves dissolution releases Nb for  $\gamma''$ , and that HIP reduces porosity while sometimes coarsening grains, so the final hardness reflects a balance between precipitation strengthening and grain-size effects. [43]

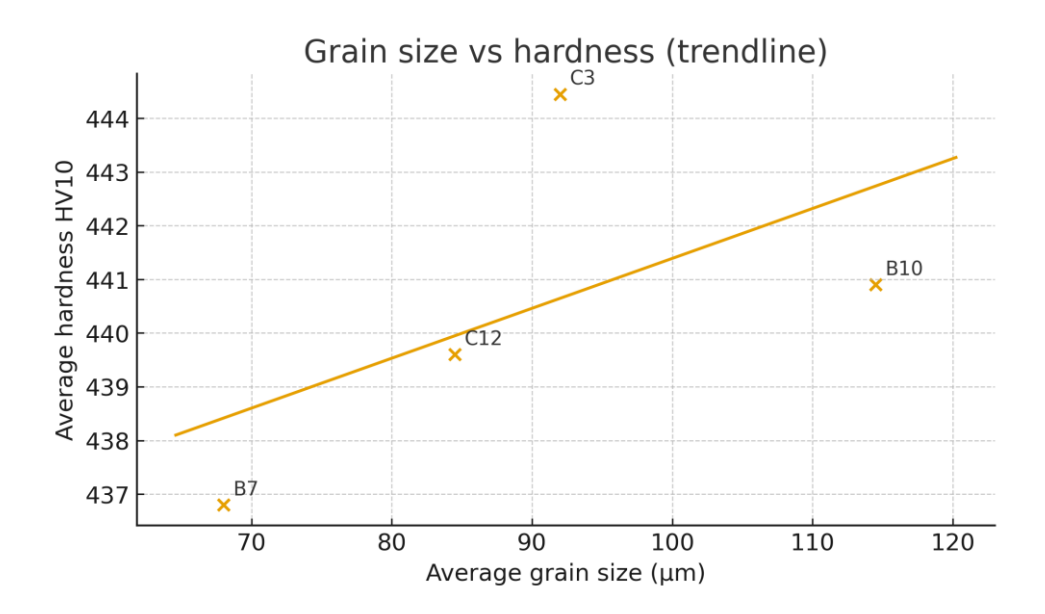


Figure 4.13: Average grain size vs average hardness (linear trendline shown).

Also, B7's smaller grains and higher NbC yield the lowest hardness (436-437 HV10), while C3's larger grains and intermediate NbC gives the highest (444 HV10). This deviation from Hall-Petch expectations is explained by, Nb partitioning into NbC reducing  $\gamma$ " availability, the primary strengthening phase. Higher porosity in B7 (0.062-0.085%) depressing local hardness figure 4.13,4.12, whereas C3 optimizes  $\gamma$ ", residual stress, and porosity defects and thus having a better life. Analysis reveals B7's high NbC pins grains but limits  $\gamma$ " and, with higher porosity, lowers HV10; B10's low NbC allows coarser grains but preserves Nb for  $\gamma$ "; C3 balances these for optimal mechanical properties.

#### Porosity measurement and influence on properties

Porosity in laser powder bed fusion (LPBF) nickel superalloys arises predominantly as:

(i) Gas pores (nearly spherical), (ii) lack-of-fusion (LoF) voids (irregular, crack-like, often inter-track/inter-layer), and (iii) keyhole pores (from unstable deep vapor cavities). Measurements on metallographic image analysis was performed on polished cross-sections taken parallel to Z (build) and in the XY plane. Pores were segmented and quantified as area fraction (%), which under stereological assumptions approximates as volume fraction. For reporting and cross-comparison, porosity can be converted to relative density = 100 – porosity (%). ASTM E1245 (automatic image analysis of second-phase constituents) for unbiased areal/volumetric fractions. Bulk density cross-checks can be done by ISO 3369/ASTM B962.

Table 4.4: Measured porosity (%) and corresponding relative density

Sample	Porosity Z (%)	Rel. density Z (%)	Porosity XY (%)	Rel. density XY (%)
C3	0.006	99.994	0.013	99.987
C12	0.026	99.974	0.022	99.978
<b>B7</b>	0.062	99.938	0.085	99.915
B10	0.013	99.987	0.016	99.984

XY sections show slightly higher porosity than Z for most samples, consistent with lack of fusion (LoF) defects aligning along layer interfaces

Fatigue is a defect-controlled life correlates far better with the largest pore's projected  $\sqrt{area}$ , shape acuity (sharp LoF vs. round gas), and proximity to the surface, then with total % porosity. This is well captured by Murakami's area parameter and numerous LPBF studies. In practice, two specimens with identical 0.02% porosity can have very different lives if one contains a single 80–120  $\mu$ m sharp LoF pore near the surface.

### 4.1 Fatigue Life Performance

Cylindrical specimens were machined to the ASTM E466 axial fatigue geometry from LPBF-built IN718 and post-heat treated as mentioned in previous section used for the rest of this work. Surface finish and gauge geometry were held consistent across all samples, so microstructural state (grain size, precipitates) and defect population (porosity) are the dominant factors influencing life in the high-cycle regime, as widely reported for LPBF IN718.

Porosity, even at less than 0.1% proportion, governs crack initiation in LPBF alloys as HIP reportedly improves fatigue by collapsing lack-of-fusion and gas pores common in additive manufactured parts. In the present study, C3 shows the lowest void fraction (0.006%) and the best life (1.24  $\times$  106 cycles at 700 MPa), while B7 despite the finest grains carries an order-of-magnitude of higher porosity (0.06-0.09%) and fails early (6  $\times$  104 cycles). These trends mirror broad evidence that defect size/density and near-surface flaws dominate High cycle fatigue in AM IN718, and that HIP + Heat treatment enhances the performance.

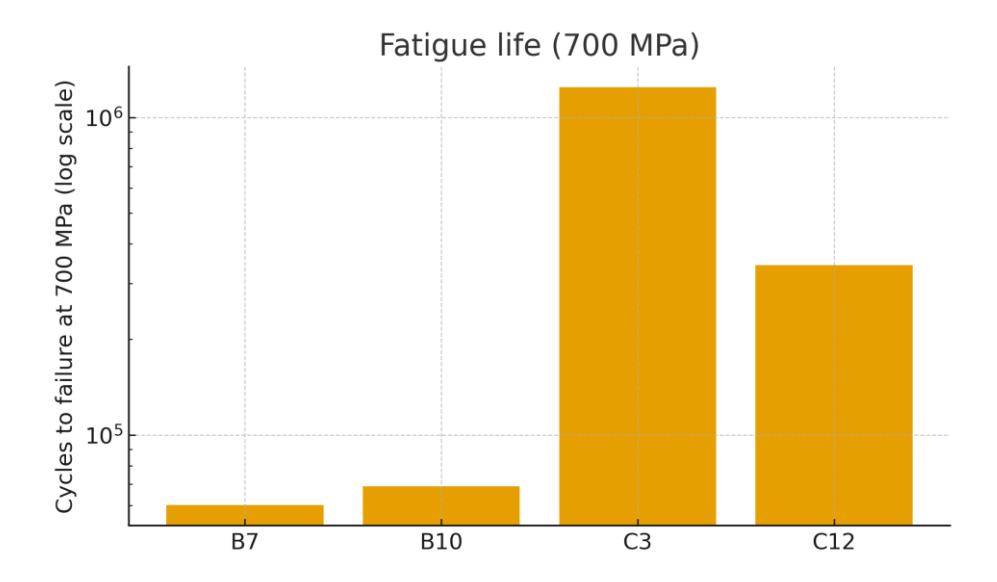


Figure 4.14: Fatigue life at 700 MPa (log scale).

At the reference stress amplitude of 700 MPa the observed fatigue life order for the four samples is:

C3 > C12 > B10 > B7. The fatigue life are graphically represented in figure 4.14.

- C3 exceeded 1.2 × 10° cycles and combines the lowest porosity (0.006-0.013%) with the highest hardness (444 HV10) and a smaller transverse grain size (79 µm), which is consistent with defect limited HCF behaviour in LPBF 718.
- C12 outperforms B10 despite its higher bulk porosity (0.022-0.026% vs 0.013-0.016%).
- **B7**, having the **highest porosity** (0.062-0.085%), ranks last even though it exhibits the finest grains (66-70 μm), underscoring the primacy of defects over modest grainsize differences in HCF for LPBF 718.

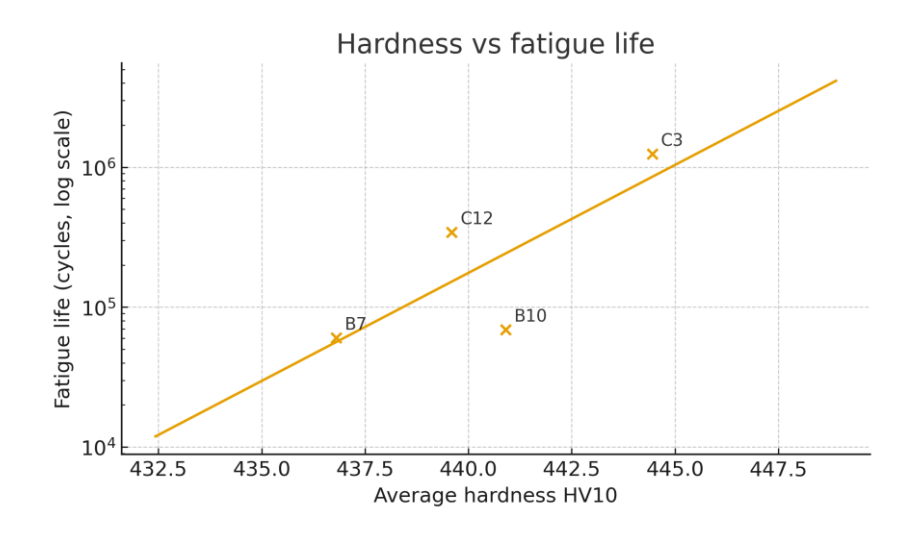


Figure 4.15: Average hardness vs fatigue life (log scale; trendline fit in log-space).

This inversion is physically reasonable under defect dominant conditions when one or more of the following apply:

- 1. Maximum defect severity & proximity to surface: HCF life correlates more strongly with the largest surface adjacent defect than with average porosity. If C12 contains fewer severity flaws at or near the free surface despite a higher average pore fraction its life can exceed B10's.
- 2. Plane-dependent porosity and build-orientation effects: C12 is the only lot where XY porosity less than Z porosity (0.022 vs 0.026%). Orientation-linked LoF morphology can reduce the probability that harmful defects intersect the gauge surface in a critical orientation, improving life even when total porosity is higher. Orientation effects have been observed to persist post-heat treatment through their influence on defect geometry and propagation behaviour.
- 3. Lower carbide-assisted crack initiation: C12 shows the lowest NbC fraction (0.28%) vs B10 (0.35%). Although pores dominate initiation statistics in LPBF 718, occasional carbide-initiated failures occur when coarse or oxidized particles reside near the surface; a lower fraction marginally reduces that risk. [52]

The measured porosity is generally higher on XY than Z for B7, B10, and C3, but not for C12. Literature shows that LoF morphology and defect alignment with the build can promote fatigue anisotropy even after standard heat treatments; therefore, defect orientation relative to the principal cyclic stress is an important co-factor when interpreting lot-to-lot performance. [53]

When defects are minimized and surfaces are well finished, LPBF IN718 can approach wrought HCF behaviour across parts of the S–N curve; differences widen in VHCF or at elevated temperatures where microstructural morphology and residual defects increasingly control thresholds and growth.

Considering all aspects together, the fatigue hierarchy is explained first by defect control (porosity), then by microstructure (grain size/anisotropy) and precipitation state. That is why C3 (HIP + aging; ultra-low porosity) outperforms B7 (fine grains but higher porosity, Nb tied in carbides) and B10 (HIPed but coarser grains).

## 5 Conclusion

This study investigated four different samples in order to find out a possible reason for one of the samples performing better in fatigue test. All of the samples were printed using Laser Powder Bed Fusion technique with the influence of hot isostatic pressing (HIP) followed by ageing treatment on the microstructure and fatigue performance of additively manufactured Nickel super-alloy Inconel IN718® specimens. The treatments were intended to reduce porosity, modify precipitate distribution, and enhance mechanical properties such as hardness and fatigue life.

The results indicate that HIP combined with ageing effectively minimizes internal porosity, promotes a more uniform precipitate strengthening phase, and refines the microstructural anisotropy, leading to improved fatigue life and hardness. These findings confirm that thermal post-treatments play a decisive role in optimizing the mechanical behavior of additively manufactured nickel-based superalloys for demanding engineering applications.

As discussed in the present study, specimen C3 have more than 1.2 million cycles of fatigue life from the test and which could be due to a combination of multiple features such as (i) ultra-low porosity (ii) high hardness 444 HV10, indicating a favourable  $\gamma''/\gamma'$  strengthening state after HIP + Aging heat treatment and a mixed anisotropy of comparatively coarser grains along Z axis which is build direction with finer XY grains that can impede straightforward crack-path continuity depending on loading direction. HIP is known to both reduce pore density and homogenizes, which tends to free Nb for  $\gamma''/\gamma'$  precipitation during subsequent aging, thereby raising cyclic strength when together these effects are strongly beneficial for fatigue performance, simulating its operational life period.

Specimen C3 (Heat Treated and HIP) with an average density of 99.99% aligns with HIP treatment and lower porosity than that of B10, C12 and B7. Since micro and nano pores are well-known crack-initiation sites that shorten fatigue life. C3's pore scarcity would have been the most significant contributor to its superior fatigue life of more than 1.2 million cycles. In the present study porosity, rather than grain refinement alone dominates failure initiation as with B7 sample's refined grains cannot compensate for ten-times higher pore content, validating crack-initiation models for AM superalloys. Grain-size anisotropy also matters as C3's fine XY grains and coarser build direction grains interrupt cracks and raise fatigue endurance compared with isotropic coarse textures in B10.

Metal Carbides such as NbC fractions could be balanced as excess carbides refine grains but deplete Nb for  $\gamma''$ , lowering hardness and life as in the case of B7, whereas insufficient carbides may permit grain growth in B10.

## 6 Limitations and future work

First, grain size alone does not fully predict strength in LPBF IN718 because nano  $\gamma''$  as a primary strengthening precipitate, texture, and porosity co-determine mechanical responses. Thus, microstructure conclusions supported by EBSD characterization for phase morphology will give a better insight. Hardness differences suggest none of the samples is severely weakened at room temperature, but the combination of higher porosity and altered precipitate balance in B7 could be detrimental for fatigue life and high temperature creep. Literatures shows that even small pockets of porosity are potent fatigue initiation sites in LPBF alloys. To reinforce causal links, pore size distribution, sphericity and location mapping using XCT, EBSD analysis for crystallographic texture and grain orientation and phase identification to confirm <001> alignment of grain growth prevalent in additive manufactured materials, a more powerful microscope for high resolution in-depth study and imaging in nanometre scale using Transmission Electron Microscope TEM/EDS to quantify  $\gamma''$  and  $\gamma'$  strengthening phases and to reveal other precipitates such as delta and laves. These steps align with current qualification frameworks and best practice in AM superalloys. Grain Boundary Character Distribution (GBCD) and Energy Anisotropy Quantifying grain boundary types (e.g. low- $\Sigma$ , high-angle, special vs. random boundaries) can provide insight into grain growth mechanisms and energy anisotropy. Furthermore, any discrepancies which would have arrived using critical software analysis and during complex methodology were taken due care and consideration with a statistical approach.

# **Bibliography**

- [1] R.C. Reed, The Superalloys: Fundamentals and Applications R. C. Reed Cambridge University Press, The Edinburgh Building, Shaftesbury Road, Cambridge. ISBN 0-521-85904-2, *The Aeronautical Journal*, vol. 112.
- [2] Additive manufacturing, explained | MIT Sloan, available at https://mitsloan.mit.edu/ideas-made-to-matter/additive-manufacturing-explained, viewed on 5 May 2025.
- [3] Bourell, D.; Stucker, B.; Spierings, A.; Herres, N.; Levy, G. Influence of the particle size distribution on surface quality and mechanical properties in AM steel parts. Rapid Prototype. J. 2011, 17, 195–202
- [4] Ferrar, B.; Mullen, L.; Jones, E.; Stamp, R.; Sutcliffe, C. Gas flow effects on selective laser melting (SLM) manufacturing performance. J. Mater. Process. Technol. 2012, 212, 355–364.
- [5] Ladewig, A.; Schlick, G.; Fisser, M.; Schulze, V.; Glatzel, U. Influence of the shielding gas flow on the removal of process by-products in the selective laser melting process. Addit. Manuf. 2016, 10, 1–9.
- [6] Cobbinah, P., Nzeukou, R., Onawale, O., & Matizamhuka, W. (2020). Laser Powder Bed Fusion of Potential Superalloys: A Review.Metals
- [7] Sims CT, StoloffNS, Hagel WC. Superalloys I1: High-Temperature Materials for Aerospace and Industrial Power. New York, USA: Wiley; 1987.
- [8] Geddes B, Leon H, Huang X. Superalloys: Alloying and performance. Materials Park Ohio: ASM International; 2010.
- [9] SAE International, 2005. AMS 5662: Inconel Alloy 718, Annealed and Aged. Warrendale, PA: SAE.
- [10] ASTM International, 2018. ASTM F3302-18: Standard Specification for Additive Manufacturing Nickel Alloy (UNS N07718) with Powder Bed Fusion. ASTM International.

- [11] Pollock, T. M., & Tin, S. 2006. Nickel-Based Superalloys for advanced turbine engines: chemistry, microstructure and properties. *Journal of Propulsion and Power*, 22(2), 361–374.
- [12] Reed, R. C. 2006. The Superalloys: Fundamentals and Applications. Cambridge University Press.
- [13] C. T. Sims, N. S. Stoloff, and W. C. Hagel, Superalloys II: High-Temperature Materials for Aerospace and Industrial Power. Wiley-Interscience, 1987.
- [14] ASM Handbook, Vol. 9: Metallography and Microstructures.
- [15] ASTM International, 2017. ASTM E3-11: Standard Guide for Preparation of Metallographic Specimens, PA: ASTM International.
- [16] ASTM International, 2007. ASTM E407-07: Standard Practice for Microetching Metals and Alloys.
- [17] ASTM International, 2013. ASTM E112-13: Standard Test Methods for Determining Average Grain Size.
- [18] ASTM International, 2017. ASTM E384-17: Standard Test Method for Microindentation Hardness of Materials.
- [19] Special Metals Corporation, Inconel alloy 718, Special Metals Corporation, Wiggin, UK, Tech. Rep, www.specialmetals.com/documents/technical-bulletins/inconel/inconel-alloy-718.pdf. Viewed on 6 April 2025.
- [20] Stainless Steel Advisory Corporation, Data sheet: Nickel-Inconel 718 (AMS 5662, UNS N07718), Stainless Steel Advisory Corporation, Tech. Rep. http://ssa-corp.com/documents/Data%20Sheet%20718-Nickel-Inconel-718-AMS-5662-UNSN07718.pdf. Viewed on 6 April 2025.
- [21] C. H. Ward and J. C. Freche, Materials data handbook: Inconel alloy 718, NASA, Cleveland, OH, USA, Tech. Rep. NASA-TM-X-68172, 1972. https://ntrs.nasa.gov/citations/19720022810
- [22] ASTM International, 2012. ASTM E1508-12: Standard Guide for Quantitative Analysis by Energy-Dispersive Spectroscopy.
- [23] ISO, 2011. ISO 22309:2011: Microbeam analysis SEM/EDS analysis of particulate matter. Geneva: International Organization for Standardization.
- [24] ASTM International 2021 ASTM F3055-14a: Standard Specification for Additive Manufacturing Nickel Alloy (UNS N07718) with Powder Bed Fusion.
- [25] G. P. Sabol and R. Stickler, Microstructure of Nickel-Based superalloys, *Physica Status Solidi (B)*, vol. 35, no. 1, pp. 11–52, Jan. 1969, doi: 10.1002/pssb.19690350102.
- [26] Lindič, M., Klobčar, D., Nagode, A., Mole, N., Pušavec, F., Kopač, J., & Šturm, R. (2025). Feasibility study of advanced manufacturing processes: Integrating LPBF and LMD for Inconel 718. Journal of Advanced Joining Processes, 11, 100239.
- [27] Lindič, M., Klobčar, D., Nagode, A., Pušavec, F., & Kopač, J. (2025). Heat treatment optimisation of 18% Ni maraging steel produced by DED-ARC for enhancing mechanical properties. Engineering Fracture Mechanics, 301.
- [28] Imširović, M., Trdan, U., Klobčar, D., Bračun, D., Nagode, A., & Berthe, L. 2024. Optimization of friction stir welding parameters for joining of Ti-Al laminated metal

- composite to AA-5754 alloy. Proceedings of the 29th International Conference on Materials and Technology (ICM&T).
- [29] Klobčar, D., Kosec, L., & Kosec, B. 2019. Comparison of the fatigue strength between additively and conventionally fabricated tool steel 1.2344. Engineering Failure Analysis, 98, 197-207.
- [30] Verma, A., Kapil, A., Klobčar, D., & Sharma, A. 2023. A review on multiplicity in multi-material additive manufacturing: Process, capability, scale, and structure. Materials, 16 (15), 5246
- [31] Balachandramurthi, A. R., Moverare, J., Dixit, N., Deng, D., & Pederson, R. 2019. Microstructural influence on fatigue crack propagation during high cycle fatigue testing of additively manufactured Alloy 718. Materials Characterization, 149, 82-94.
- [32] Gribbin, S., Ghorbanpour, S., Ferreri, N. C., Bicknell, J., Tsukrov, I., & Knezevic, M. (2019). Role of grain structure, grain boundaries, and transition bands in fatigue behavior of Inconel 718. International Journal of Fatigue, 125, 116-128.
- [33] Seede, R., Shoukr, D., Ramirez, B., Mostafa, A., Li, B., Kirka, M., ... & Ye, J. 2020. Microstructural and microhardness variations with respect to height in Inconel 718 parts fabricated by laser powder bed fusion. Journal of Manufacturing Processes, 58, 1161-1171.
- [34] Witkin, D. B., Albright, T. V., & Patel, D. (2020). Empirical approach to understanding the fatigue behavior of metals made using additive manufacturing. Metallurgical and Materials Transactions A, 51, 2186-2194.
- [35] Balachandramurthi, A. R., Moverare, J., Mahade, S., & Pederson, R. 2021. Additive manufacturing of Alloy 718 via electron beam melting: Effect of post-treatment on the microstructure and high-temperature mechanical properties. Materials, 14(3), 715
- [36] Goel, S., Bourreau, K., Olsson, J., Klement, U., & Joshi, S. 2021. Mechanical and microstructural behavior of additively manufactured Inconel 718 with subsequent heat treatments. Materials Science and Engineering: A, 805, 140600.
- [37] Sanchez, S., Gaspard, G., Hyde, C. J., Ashcroft, I. A., Ravi, G. A., & Clare, A. T. (2021). The interplay between vaporisation, low melting point constituents and the metallurgical reactions with impurities in the laser powder bed fusion of Alloy 718. Additive Manufacturing, 4, 101966.
- [38] M. Sundararaman, P. Mukhopadhyay, and S. Banerjee, Precipitation of the δ-Ni3Nb phase in two nickel base superalloys, *Metallurgical Transactions A*, vol. 19, no. 3, pp. 453–465, 1988.
- [39] Watring, D. S., Benzing, J. T., Hrabe, N., & Lance, M. J. 2022. Effects of laser-energy density and build orientation on the structure–property relationships in as-printed AlSi10Mg processed by laser powder bed fusion. Additive Manufacturing, 36, 101425
- [40] Zhang, F., Levine, L. E., Allen, A. J., Stoudt, M. R., Lindwall, G., Lass, E. A., ... & Cleary, M. E. (2018). Effect of heat treatment on the microstructural evolution of a nickel-based superalloy additive-manufactured by laser powder bed fusion. Acta Materialia, 152, 200-214.
- [41] Zhao, Y., Li, Y., Gao, P., Zhang, B., Feng, K., Huang, J., ... & Wu, Z. (2024). Effect of microstructure and crystallographic texture on the fracture toughness anisotropy of LPBF IN718. Materials, 18(16), 3737.

- [42] Y. Zhao, K. Li, M. Gargani, and W. Xiong, A comparative analysis of Inconel 718 made by additive manufacturing and suction casting: Microstructure evolution in homogenization, *Additive Manufacturing*, vol. 36, p. 101404, Jun. 2020, doi: 10.1016/j.addma.2020.101404.
- [43] Y. Zhao and W. Xiong, Influence of Homogenization on Phase Transformations during Isothermal Aging of Inconel 718 Superalloys Fabricated by Additive Manufacturing and Suction Casting, *Materials*, vol. 16, no. 14, p. 4968, Jul. 2023, doi: 10.3390/ma16144968.
- [44] A. Mitchell, A.J. Schmalz, C. Schvezov and S.L. Cockcroft. The Precipitation of Primary Carbides in Alloy 718. University of British Columbia, Vancouver, B.C., Canada, V6T 124
- [45] Li, Z., Xu, R., Zhang, Z., Cui, Y., & Li, Y. Study on microstructure and fatigue properties of laser powder bed fusion Inconel 718 in the long-life regime. Additive Manufacturing Frontiers, 4, 200148.
- [46] A. Chamanfar, H. Monajati, A. Rosenbaum, M. Jahazi, A. Bonakdar, and E. Morin, Microstructure and mechanical properties of surface and subsurface layers in broached and shot-peened Inconel-718 gas turbine disc fir-trees, *Materials Characterization*, vol. 132, pp. 53–68, Aug. 2017.
- [47] E. A. Loria, Superalloy 718: Metallurgy and Applications: Proceedings of the International Symposium on the Metallurgy and Applications of Superalloy 718. 1989.
- [48] John F. Radavich, The Physical Metallurgy Of Cast And Wrought Alloy, School of Materials Engineering, Purdue University 1989.
- [49] J. Radhakrishnan, P. Kumar, S. Li, Y. Zhao, and U. Ramamurty, Unnotched fatigue of Inconel 718 produced by laser beam-powder bed fusion at 25 and 600°C, *Acta Materialia*, vol. 225, p. 117565, Dec. 2021.
- [50] T. G. Gallmeyer, S. Moorthy, B. B. Kappes, M. J. Mills, B. Amin-Ahmadi, and A. P. Stebner, "Knowledge of process-structure-property relationships to engineer better heat treatments for laser powder bed fusion additive manufactured Inconel 718," *Additive Manufacturing*, vol. 31, p. 100977, Nov. 2019.
- [51] Timothy M. Smith, Timothy P. The effect of composition on microstructure and properties for IN718, additively manufactured superalloy. NASA Technical Reports Server, NTRS
- [52] E. Sadeghi *et al.*, A state-of-the-art review on fatigue performance of powder bed fusion-built alloy 718, Progress in Materials Science, vol. 133, p. 101066, Dec. 2022.
- [53] A. R. Balachandramurthi *et al.*, On the Microstructure of Laser Beam Powder Bed Fusion Alloy 718 and Its Influence on the Low Cycle Fatigue Behaviour, *Materials*, vol. 13, no. 22, p. 5198, Nov. 2020.
- [54] MDS EOS NickelAlloy IN718, EOS GmbH, Apr. 09, 2025. Available at: https://www.eos.info/metal-solutions/metal-materials/data-sheets/mds-eos-nickelalloy-in718, viewed on 7 March 2025.
- [55] Metallographic cutting insight. Avaliable at: https://www.struers.com/en/Knowledge/Cutting. Viewed on 9 March 2025.

- [56] ASTM E3-11(2017)-Standard Guide for Preparation of Metallographic Specimens
- [57] Metallographic mounting insight | Available at: https://www.struers.com/en/Knowledge/Mounting. Viewed on 9 March 2025.
- [58] Metallographic grinding and polishing insight | Struers.com. Available at : https://www.struers.com/en/Knowledge/Grinding-and-polishing. Viewed on 9 March 2025.